Title: **Dynamical modeling reveals RNA decay mediates the effect of matrix stiffness on aged muscle stem cell fate**

Authors: Zachary R. Hettinger[1,2,3], Sophia Hu[4,5], Hikaru Mamiya[6,7], Amrita Sahu[6], Hirotaka Iijima[6,#], Kai Wang[1,2,6], Gabrielle Gilmer[1,2,8,9], Amanda Miller[6], Gabriele Nasello[10], Antonio D'Amore[10], David Vorp[7,10,12], Thomas A. Rando[13,14,15], Jianhua Xing[4,5,16,17], Fabrisia Ambrosio[1,2*]

Affiliations:
[1]Department of Physical Medicine and Rehabilitation, Harvard Medical School. Boston, MA, USA.
[2]Discovery Center for Musculoskeletal Recovery, Schoen Adams Research Institute at Spaulding. Boston, MA, USA.
[3]Department of Geriatric Medicine, University of Pittsburgh. Pittsburgh, PA, USA.
[4]Department of Computational and Systems Biology, University of Pittsburgh. Pittsburgh, PA, USA.
[5]CMU-Pitt PhD Program in Computational Biology, University of Pittsburgh. Pittsburgh, PA, USA.
[6]Department of Physical Medicine and Rehabilitation, University of Pittsburgh. Pittsburgh, PA, USA.
[7]Department of Bioengineering, University of Pittsburgh. Pittsburgh, PA, USA.
[8]Cellular and Molecular Pathology Graduate Program, University of Pittsburgh. Pittsburgh, PA, USA
[9]Medical Scientist Training Program, University of Pittsburgh. Pittsburgh, PA, USA.
[10]Department of Surgery, University of Pittsburgh. Pittsburgh, PA, USA.
[11]Department of Environmental and Occupational Health, University of Pittsburgh. Pittsburgh, PA, USA.
[12]Department of Mechanical Engineering and Materials Science, University of Pittsburgh. Pittsburgh, PA, USA.
[13]Veterans Affairs Palo Alto Health Care System. Palo Alto, CA, USA.
[14]Department of Neurology and Neurological Sciences, Stanford University School of Medicine. Stanford, CA, USA.
[15]Broad Stem Cell Research Center, University of California Los Angeles. Los Angeles, CA, USA.
[16]UPMC-Hillman Cancer Center, University of Pittsburgh. Pittsburgh, PA, USA.
[17]Department of Physics and Astronomy, University of Pittsburgh. Pittsburgh, PA, USA.

***Corresponding Author:** Fabrisia Ambrosio, PhD, MPT
Suite 5.303, MGH CNY 149. 149 13th St, Charlestown, MA 02129
Phone: (412) 657-1525
Email: fambrosio@mgh.harvard.edu

[#] Current Institution: Institute for advanced research, Nagoya University, Nagoya, Japan. Biomedical and Health Informatics Unit, Graduate School of Medicine, Nagoya University, Nagoya, Japan.

Graphical Abstract:

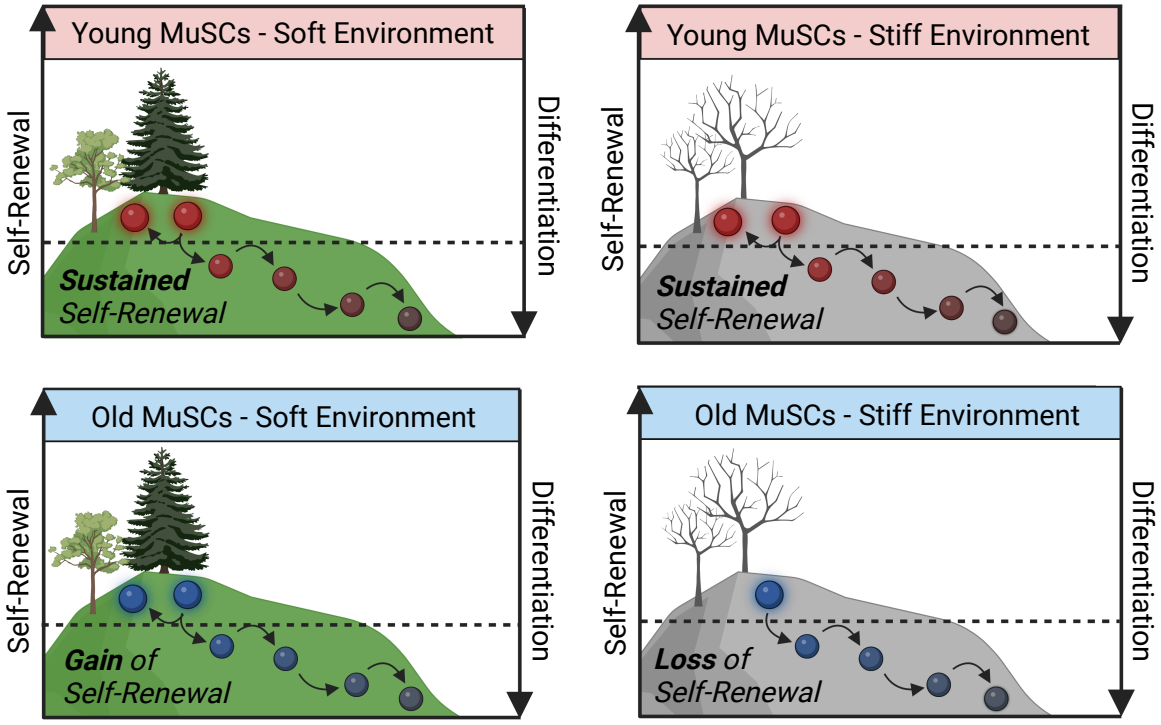

Graphical abstract description: The balance of self-renewal and differentiation in young muscle stem cells (MuSCs) is robust to perturbations of the biophysical microenvironment. In contrast, aged MuSCs are highly sensitive to extrinsic perturbations, and exposure to a youthful microenvironment rejuvenates the self-renewing potential of aged MuSCs by modulating post-transcriptional RNA dynamics.

Summary:

Loss of muscle stem cell (MuSC) self-renewal with aging reflects a combination of influences from the intracellular (e.g., post-transcriptional modifications) and extracellular (e.g., matrix stiffness) environment. Whereas conventional single cell analyses have revealed valuable insights into factors contributing to impaired self-renewal with age, most are limited by static measurements that fail to capture nonlinear dynamics. Using bioengineered matrices mimicking the stiffness of young and old muscle, we showed that while young MuSCs were unaffected by aged matrices, old MuSCs were phenotypically rejuvenated by young matrices. Dynamical modeling of RNA velocity vector fields *in silico* revealed that soft matrices promoted a self-renewing state in old MuSCs by attenuating RNA decay. Vector field perturbations demonstrated that the effects of matrix stiffness on MuSC self-renewal could be circumvented by fine-tuning the expression of the RNA decay machinery. These results demonstrate that post-transcriptional dynamics dictate the negative effect of aged matrices on MuSC self-renewal.

Running Title: Stiffness drives mRNA decay in aged muscle stem cells

Keywords: Aging, stem cells, cell fate, stiffness, RNA decay, skeletal muscle

102 **Introduction:**

103 Skeletal muscle regenerative capacity steadily declines with age due to a compromised ability of
104 muscle stem cells (MuSCs) to repair injured muscle and replenish their niche (1, 2). Whereas
105 aberrant lineage specification of aging stem cells has typically been assessed using static
106 measures such as transcript or protein levels, dynamical cell state properties suggests that fate
107 decisions may represent a transition between distinct "attractors", as has been analogized by
108 Waddington's landscape (3, 4). Inspired by dynamical systems theory, Waddington depicts the
109 path taken by a marble (i.e., cell) as it rolls down a hill (i.e., the cellular landscape) to represent
110 cellular progression from an undifferentiated to a differentiated state (4). Bifurcations along the
111 path of the marble represent alternative fates. Extending the metaphor, a less common scenario
112 in which the cell starts the path to differentiation but then changes direction to roll up the hill
113 represents a reversion to an undifferentiated state, or self-renewal. Associated with, and perhaps
114 contributing to, Waddington's epigenetic landscape is the physical landscape of the stem cell
115 niche. Here we asked, *how does the MuSC physical landscape change over time and how do*
116 *age-related changes to the MuSC landscape affect cellular fate transitions?*
117
118 One prominent aspect of the MuSC physical landscape is the extracellular matrix (ECM). ECM
119 mechanical properties represent well-established drivers of stem cell fate, as evidenced by a
120 series of elegant *in vitro* studies demonstrating regulation of stem cell lineage progression via
121 extrinsic mechanical signals (5, 6). For instance, mesenchymal stem cells spontaneously
122 differentiated toward a myogenic lineage when seeded on a soft substrate engineered to mimic
123 the compliance of young, healthy muscle (elastic modulus €: 8 – 17 kPa) (5). On the other hand,
124 osteogenic differentiation was observed when cells were seeded on a stiffer substrate (€: 25 – 40
125 kPa) (5). Given biophysical characteristics of the ECM are altered with aging (7-9), these *in vitro*
126 findings underscore the potential impact of age-associated changes to the ECM on MuSC lineage
127 specification *in vivo*.
128
129 Aged muscle is typically characterized by abnormal ECM deposition and remodeling, contributing
130 to increased tissue stiffness (10-14). Indeed, recent studies from our laboratory have shown
131 decreased collagen tortuosity and a concomitant increase in muscle rigidity along the axis of
132 collagen fibrils in aged muscle (8). These age-related ECM alterations have direct effects on
133 MuSC lineage specification, as we have previously shown MuSCs seeded onto decellularized
134 ECM from aged muscle display an increased fibrogenic conversion compared to cells placed on
135 ECM derived from young muscle (8). However, the cell state regulatory mechanisms that underlie

136 age- and stiffness-dependent MuSC fate decisions are poorly understood. In this study, we tested
137 the hypothesis that age-related alterations in stiffness of the skeletal muscle ECM compromise
138 MuSC lineage progression. Specifically, we employed an array of single cell approaches at the
139 morphological, protein, and RNA levels to determine whether the biophysical properties of the
140 aged muscle physical landscape predispose MuSCs towards differentiation, to test whether the
141 properties of a young niche restore self-renewal in old MuSCs, and to interrogate mechanisms by
142 which MuSCs adopt aberrant fate kinetics upon exposure to an aged niche.
143
144
145 **Results:**
146 **Age-related matrix stiffness is associated with aberrant MuSC nuclear morphologies**
147 While numerous reports have highlighted profound age-related biochemical changes to the
148 skeletal muscle ECM (8, 15, 16), comprehensive biophysical characterizations are fewer in
149 number (17). Quantification of the micromechanical properties of muscle is challenging due to the
150 unique ECM architecture and a lack of standardized methodology (18). Moreover, uniaxial testing
151 is limited because it does not capture the out-of-plane properties of muscle (18). To overcome
152 these limitations, we modeled biaxial microscale muscle stiffness using macroscale
153 measurements collected from young (4-6 months) and old (22-24 months) male mice (**Fig. 1A**).
154 The fibril network architectural features of young and old muscle were used to create artificial fiber
155 networks that were stochastically equivalent to experimental samples. On the artificial network,
156 we applied a structural deterministic approach to derive the single fiber Green's strain, as
157 previously described (18). From these data, we performed a finite element simulation of fiber
158 network mechanical behavior to predict microscale stiffness from our macroscale measurements
159 (**Fig. 1A**). We found that aged muscle stiffness was increased compared to young counterparts,
160 as evidenced by a significantly reduced Green's strain deformation (**Fig. 1B**). Using previously
161 published formulae (19, 20), fiber mesh model predictions from experimentally-derived biaxial
162 data revealed that aged muscle is approximately 3.5-fold stiffer than young muscle. (**Fig. 1C**).
163
164 Cells respond to mechanical cues through cytoskeletal remodeling, nuclear deformation, and
165 chromosomal reorganization to modulate gene expression dictating cell fate (i.e., activation,
166 proliferation, and/or differentiation) (21, 22). We therefore evaluated how age-related stiffness
167 impacts the nuclear morphology of muscle mononuclear cells. To do this, we utilized *in situ* and
168 *ex vivo* approaches to characterize nuclear morphologies using both standard fluorescence
169 microscopy and image-based flow cytometry (ImageStream; ISX). A mask was placed over DAPI-

170 stained mononucleated cells from muscle cross-sections, and images were assessed for a variety
171 of nuclear morphological variables using CellProfiler™ (23) (**Fig. 1D**). Unsupervised principal
172 component analysis (PCA) followed by supervised linear discriminant analysis (LDA) of all nuclear
173 morphological variables (*N*=56) revealed that young and old cells display distinct morphologies,
174 as evidenced by age-specific clustering of cells (**Fig. 1E, 1F**). Features contributing to clustering
175 were largely attributed to significant differences in the nuclear area, solidity (i.e., roundness), and
176 compactness (i.e., nuclear integrity) of old nuclei compared to young (**Fig. 1G**).
177
178 To corroborate the above findings with nuclear morphologies of isolated MuSCs specifically, we
179 performed fluorescence-activated cell sorting of integrin subunit alpha 7-positive cells (*Itga7*+)
180 followed by DAPI staining and imaging using ISX (**Fig. 1H**). PCA-LDA analyses using nuclear
181 morphological features obtained from young and old MuSCs revealed a similar segregation of
182 clusters according to age as compared to our *in-situ* findings (**Fig. 1I, 1J**). The primary features
183 driving segregation of the clusters included nuclear area, aspect ratio (i.e., roundness), and
184 gradient RMS (i.e., texture/granularity) (**Fig. 1K**). Taken together, these data demonstrate that
185 elevated stiffness of aged muscle is associated with an altered nuclear morphology of MuSCs, *in*
186 *situ* and *ex vivo*.
187
188 **Reducing matrix stiffness restores a more youthful cell state to old MuSCs**
189 Given that nuclear architecture is a significant predictor of MuSC activation and proliferative
190 potential (24), we hypothesized that the increased stiffness and altered nuclear morphology of old
191 MuSCs contributes to aberrant lineage specification following activation. To test this hypothesis,
192 we isolated and cultured young and old MuSCs on fabricated polydimethylsiloxane (PDMS)
193 substrates calibrated to approximate the physiological stiffness of young (soft; 12 kPa) and old
194 (stiff; 29 kPa) muscle, after which we performed morphometric analysis using ISX (**Fig. 2A**). A
195 combination of 8 nuclear morphological variables were used as input for PCA-LDA analyses,
196 which demonstrated no stiffness-related clustering of young MuSCs cultured on either soft or stiff
197 substrates (**Fig. 2B, 2C**). In contrast, old MuSCs cultured on a soft, but not a stiff, substrate
198 showed tight clustering (**Fig. 2D, 2E**). Interrogation of variables contributing to LDA analyses
199 revealed there were no differences in young MuSCs for any of the measured variables, regardless
200 of matrix condition. In contrast, LDA was significantly different when comparing old MuSCs
201 seeded onto soft versus substrates (**Fig. 2E)**. Accordingly, we observed a significant reduction in
202 the nuclear area in old MuSCs on soft substrates compared to stiff (**Fig. 2F, 2G**).
203

204 To determine whether changes in the nuclear morphology of old MuSCs on soft substrates are
205 accompanied by changes in cell state markers, we next performed ISX of MuSC lineage markers
206 corresponding to quiescence (Pax7+/Myod-), activation and/or cycling (Pax7+/MyoD+), and
207 differentiation (Pax7-/MyoD-). As was the case for morphological metrics, we observed no
208 differences in relative marker expression in young MuSCs on soft versus stiff matrices (**Fig. 2H**).
209 However, old MuSCs were highly sensitive to matrix condition, as soft substrates increased the
210 percentage of activated/cycling old MuSCs compared to cells cultured on stiff substrates (43%
211 vs. 21%, respectively; **Fig. 2H**). The fraction of differentiated MuSCs (Pax7-/MyoD-) was also
212 reduced when old MuSCs were cultured on soft substrates as compared to a stiff substrate (37%
213 vs. 54%, respectively; **Fig. 2H**). These data suggest stability in the young MuSC phenotype,
214 regardless of substrate stiffness. Old MuSCs, however, are highly responsive to extrinsic
215 biophysical cues, whereby reduced matrix stiffness promoted an increased number of activated
216 and cycling cells.
217
218 To explore the potential physiological relevance of the above findings, we next pharmacologically
219 manipulated the mechanical properties of skeletal muscle in aged mice using β-aminopropionitrile
220 (BAPN). BAPN is a chemical inhibitor of lysyl oxidase (LOX), an enzyme responsible for the age-
221 related accumulation of crosslinked collagen and elevated tissue stiffness, not only in skeletal
222 muscle (9), but also in the lungs, heart, and bone (25-28). We performed daily subcutaneous
223 injections of BAPN for a total of six weeks in young and old mice. Four weeks following the start
224 of BAPN injections, animals received cardiotoxin injections bilaterally in tibialis anterior muscles
225 (**Fig. 2I**). We hypothesized that decreased matrix cross-linking and, by extension, matrix stiffness
226 (29), would improve the regenerative capacity of aged muscle following an injury. Two weeks
227 after recovery from injury, aged mice that received BAPN exhibited improved regeneration,
228 evidenced by increased regenerating fiber cross-sectional area (CSA), increased force producing
229 capacity, and a reduced refractory period following stimulation (**Fig. 2J-2M**). Collectively, these
230 results corroborate our *in vitro* findings and demonstrate that manipulation of the aged MuSC
231 microenvironment benefits functional skeletal muscle regeneration *in vivo*.
232
233 **Post-transcriptional dynamics contribute to stiffness-mediated lineage specification**
234 Thus far, our results have shown that reducing substrate stiffness impacts the activated and
235 cycling fraction of old MuSCs, which may be reflective of enhanced self-renewal. As such, we
236 sought to better understand the molecular mechanisms constituting these changes. To do this,
237 we performed single cell RNA sequencing (scRNA-seq) and *in silico* lineage analysis of young

238 and old MuSCs on soft and/or stiff substrates. Following cell/transcript quality control and filtration
239 of technical artifact (**Fig. S1A-E**), dimensionality reduction and trajectory analyses of MuSCs were
240 performed using Monocle 3.0 (30) (**Fig. 3A**). Monocle 3.0 is a lineage analysis algorithm that
241 organizes cells based on cell state to identify cellular lineage progression (30, 31). Dimensionality
242 reduction using PCA and UMAP visualization of MuSCs showed no differences in clustering as
243 compared to Monocle 3.0 trajectory projections (**Fig. SF-H**). Therefore, we focused our
244 subsequent analyses of MuSCs using Monocle 3.0 alone.
245
246 Analyzing MuSCs from all four groups in aggregate (i.e., young/old, and soft/stiff MuSCs),
247 trajectory analyses identified a myogenic continuum originating from MuSCs with the highest
248 expression of MuSC marker, *Pax7*, and then bifurcating towards either a self-renewing or a
249 differentiating trajectory (**Fig. 3A, S2I**). Following unbiased graph-based clustering, a total of four
250 distinct subpopulations of MuSCs were identified along each trajectory, which we labeled
251 "Cycling" and "Activated" as part of the self-renewing trajectory, and "Early Differentiation", and
252 "Late Differentiation" as part of the differentiating trajectory (**Fig. 3A, 3B**). The validity of
253 subpopulation classification was demonstrated by high expression of genes that have been
254 previously shown to be indicative of each cell state (i.e., Activated-*Fn1*^{Hi}, Cycling-
255 *Ccnd1*^{Hi}/Ccnb1^{Hi}/Ccne1^{Hi}, Early Differentiation-*Myog*^{Hi}/Hdac11^{Hi}, and Late Differentiation-*Myh3*^{Hi};
256 (32-35)) (**Fig. 3A1-3A3, 3B**). Moreover, self-renewing genes were highly expressed towards the
257 start of pseudotime, while differentiating genes were highly expressed by the end of pseudotime.
258 When cells were segregated according to group (i.e., young versus old on soft versus stiff),
259 trajectory analysis revealed that, as expected, young MuSCs displayed both self-renewing and
260 differentiating trajectories, regardless of the substrate stiffness (**Fig. 3C-3E**), though a stiff
261 substrate did introduce a bifurcation in each direction. That is, we observed an additional branch
262 in both the self-renewing and differentiation trajectories (**Fig. 3E)**. Such bifurcations are indicative
263 of increased complexity of the parent trajectory (30). In contrast, we found that old MuSCs
264 displayed relative transcriptional rigidity, adopting only a single lineage towards differentiation on
265 both soft and stiff substrate conditions (**Fig. 3C, 3F, 3G**). The number of cycling old MuSCs, while
266 not altogether absent, was insufficient to constitute a bona fide self-renewing trajectory,
267 regardless of whether cells were seeded onto a soft or stiff substrate (**Fig. 3C, 3F, 3G**). Similar to
268 lineage analyses using Monocle 3.0, there were no significant differences in differential gene
269 expression for old MuSCs seeded on soft versus stiff substrates (**Fig. S2K)**. We found this
270 observation surprising given that old MuSCs seeded onto soft substrates displayed a phenotype

271 indicative of enhanced self-renewal when compared to old cells seeded on a stiff substrate (**Fig.**
272 **2H**).
273
274 The above findings suggest a disconnect between morphological/protein level changes and those
275 at the transcriptional level. This is consistent with previous observations showing that steady-state
276 *(static)* measures of RNA abundance often fail to correlate with protein levels (36-38). As an
277 alternative, a growing number of studies have demonstrated that post-transcriptional gene
278 regulation plays an underappreciated role in shaping the proteome (39). We therefore posited
279 that non-steady-state *(dynamic)* RNA metrics may better capture the transcriptional changes
280 mediating the phenotypic responses of old MuSCs on a soft matrix. RNA velocity provides such
281 a metric by accounting for the relationship between the relative abundance of both unspliced and
282 spliced RNA, thereby providing estimated rates of splicing and degradation (40). As evidence of
283 the distinct features captured by dynamic versus static approaches, PCA revealed only a single
284 cluster when considering static gene counts, indicating few differences across the four
285 experimental groups (**Fig. 3H**). In contrast, RNA velocity yielded a total of six clusters
286 corresponding to cell state, age, and matrix condition (**Fig. 3I**). Post-transcriptional regulators
287 DEAD-box helicase 27 (*Ddx27*) and ubiquitin specific peptidase 39 (*Usp39*) serve as just two
288 examples of such a distinction between static versus dynamic assessments (**Fig. S2L)**.
289
290 When considering RNA velocity, old MuSCs on soft versus stiff substrates diverged in the
291 activated and cycling cluster of cells, while the differentiating group of cells on each substrate
292 condition were overlapping (**Fig. 3I**). To investigate whether cluster segregation was the result of
293 impaired old MuSC self-renewing potential and a predisposition towards differentiation, we
294 inferred the future states of cycling and activated old MuSCs using phase portraits. Phase
295 portraits delineate whether transcripts are considered to be in steady-state, increased velocity
296 (i.e., an increased abundance of unspliced to spliced transcripts), or decreased velocity (i.e., an
297 increased abundance of spliced to unspliced transcripts) (40). Phase portraits for early
298 differentiation marker, myogenin (*Myog*), and late differentiation marker, *Myh3*, revealed
299 increased velocity for each marker in old MuSCs on stiff substrates (**Fig. 3J**). Old MuSCs on soft
300 substrates, however, showed relatively few unspliced or spliced transcripts of either marker,
301 suggesting that soft matrices maintain a self-renewing state for old MuSCs. One interpretation of
302 these results is that, while static modeling identified negligible differences in old MuSC trajectories
303 when considering soft versus stiff substrates, dynamical modeling revealed that stiff substrates
304 predispose old MuSCs towards differentiation while soft substrates preserve a self-renewing

305 state. These data raised the hypothesis that the effect of substrate stiffness on old MuSC lineage
306 progression may be primarily mediated through post-transcriptional mechanisms.
307
308 **Soft matrices reduce RNA decay pathway activity to preserve self-renewal in old MuSCs**
309 To further investigate lineage specification trajectories using RNA velocity, we leveraged *dynamo*,
310 a robust machine learning framework that utilizes RNA velocity of the cell's transcriptome to
311 reconstruct continuous velocity vector fields (41). *Dynamo* not only provides insight into the future
312 state of cells through visualization of RNA velocity vector fields, but it also uses differential
313 geometry analysis to identify the "attractors" that govern cell gravitation towards state-specific
314 stable points. Attractors represent nodes to which cells converge along the trajectory, thereby
315 reflecting deterministic lineage specification tendencies. Using this approach, we evaluated
316 whether reducing matrix stiffness influences the stability and/or presence of "attractors" related to
317 self-renewal in old MuSCs (**Fig. 4A**).
318
319 Following vector-field generation, we observed numerous single cell trajectories (indicated by
320 vector orientation) for young and old MuSCs on each substrate condition, with attractors identified
321 in various intermediate cell states (**Fig. 4B1-4**). In contrast to static expression-based
322 approaches, *dynamo* revealed age-, substrate-, and subpopulation-dependent stable points
323 (attractors) for both young and old MuSCs on each substrate condition (**Fig. 4B1-4**). Young
324 MuSCs exposed to soft versus stiff substrates demonstrated similar attractor profiles, with
325 subpopulations that spanned both self-renewing and differentiation trajectories (**Fig. 4B1-2**).
326 These analyses are consistent with our previous findings demonstrating the resilience of young
327 MuSCs even when exposed to a stiff matrix (**Fig. 3E**). The attractors for old MuSCs on a stiff
328 substrate indicated a predisposition of towards differentiation (**Fig. 4B4**). However, on a soft
329 substrate, new stable points in the activated and cycling states of old MuSCs emerged,
330 suggesting enhanced self-renewal (**Fig. 4B3**).
331
332 To identify genes driving the attraction of old MuSCs seeded on a soft, but not stiff, matrix towards
333 self-renewing intermediate cell states, we performed random forest classifications (42). Random
334 forests identified a discrete gene set with corresponding differential RNA velocities between the
335 two groups. Functional gene set enrichment analyses summarized these genes to be highly
336 associated with nonsense mediated RNA decay (NMD) and the cellular stress response (43-46)
337 (**Fig. 4C)**. The velocities of nearly all identified genes were reduced in old MuSCs on soft matrices
338 relative to stiff matrices, suggesting that an aged microenvironment enhances effectors of stress

339 and RNA decay (**Fig. S2A**). To determine potential transcription factors mediating the activation
340 of the stress response and RNA decay in old MuSCs on stiff matrices, we overlaid the gene set
341 identified above with a curated database of known transcription factor (TF) – target gene pairs
342 using TRANSFAC (47). The TF most associated with the identified genes was ETS Like-1 protein
343 Elk-1 (*Elk1*), a member of the stress-activated protein kinase superfamily and relative of p38
344 mitogen-activated protein kinase (MAPK) (**Fig. S2B**) (45). P38 MAPK is a known contributor to
345 the loss of self-renewal and stemness in old MuSCs (48). It is worthwhile to note that there were
346 no differences in *Elk1* when considering static gene expression levels between old MuSCs
347 exposed to either soft or stiff matrices (**Fig. 4D**). In contrast, *Elk1* displayed increased velocity at
348 the boundary between activated and differentiating lineages for old MuSCs (**Fig. 4E**). Given
349 increased velocity suggests an increased rate of splicing and, therefore, a greater number of
350 mature transcripts, these findings suggest a potential relationship between matrix stiffness, the
351 cellular stress response, and subsequent changes in cell fate. Importantly, there was an overall
352 decrease in *Elk1* RNA velocity in old MuSCs on soft substrates compared to stiff, implying reduced
353 activation of cellular stress and RNA decay (**Fig. 4E**). Together, these data suggest that the
354 emergence of stable points in states related to self-renewal for old MuSCs on a soft substrate
355 may be attributed to decreased stress activation and RNA degradation.
356
357 Does RNA decay mediate the effects of age-related matrix stiffness on old MuSC fate? To answer
358 this question, we applied the perturbation feature in *dynamo,* which leverages the vector field
359 Jacobian. This approach allows genes of interest (GOIs) to be computationally tuned to observe
360 how the velocities of the remaining genes change, and subsequently how lineage progression is
361 affected. In this way, we can determine how GOIs control lineage specification trajectories of the
362 MuSC population. This *in silico* approach was therefore used to test our hypothesis that stiff
363 matrices increase RNA degradation and promote differentiation of old MuSCs, while soft matrices
364 reduce RNA decay to preserve self-renewal (**Fig. 4G**). Since NMD machinery is a complex
365 arrangement of proteins that have redundant roles in RNA degradation, we manipulated
366 expression of a foundational NMD scaffold protein, LSM14a mRNA processing body assembly
367 factor (*LSM14a*), which is responsible for housing and protecting NMD effectors (49) (50, 51) (**Fig.
368 4F**). We hypothesized that computational inhibition of *LSM14a* in old MuSCs on stiff matrices
369 would decrease RNA decay and restore self-renewal, thus inducing a more youthful lineage
370 trajectory profile. Conversely, we hypothesized that computational overexpression of *LSM14a* in
371 old MuSCs on soft matrices would reinforce vectors towards differentiation, thereby abrogating
372 the beneficial effect of a soft matrix on old MuSC self-renewal (**Fig. 4G**).

373 *In silico* downregulation of *LSM14a* caused the trajectories of old MuSCs cultured on stiff matrices
374 to reverse vector fields, predisposing cells away from differentiation in favor of an undifferentiated,
375 self-renewing state (**Fig. 4H**). Characterization of genes upregulated by computational inhibition
376 of *LSM14a* revealed an enrichment of biological processes related to cellular division and mitosis,
377 including increased expression of self-renewal genes such as H2a histone family member Z
378 (*H2afz*) and syndecan-4 (*Sdc4*) (52-54) (**Fig. 4I**). Biological processes downregulated as a result
379 of reduced *LSM14a* expression were related to muscle contraction, with corresponding reduced
380 expression of myosin heavy chain gene isoforms including -1, -3, and -7 (*Myh1, Myh3, Myh7*,
381 respectively) (**Fig. 4I**). On the other hand, *in silico* upregulation of *LSM14a* in old MuSCs on soft
382 matrices altered the direction of vectors away from a cycling, activated, and early differentiated
383 state and towards a fully differentiated one (**Fig. 4J**). Consistent with this overall trend,
384 characterization of biological processes up- and down-regulated with *LSM14a* upregulation
385 revealed enrichment of processes associated with muscle cell differentiation and mitosis,
386 respectively (**Fig. 4K**). To rule out the possibility that these findings are age-dependent, we
387 performed the same perturbations in young MuSCs. We observed that upregulation of *LSM14a*
388 in young MuSCs on soft matrices had similar effects as were observed in old cells, that is an
389 aversion from self-renewing trajectories towards differentiation (**Fig. S2C**). Taken together with
390 protein and morphological-level assessments, these results demonstrate that age-related
391 increases in matrix stiffness stimulate activation of RNA decay pathways, predisposing MuSCs
392 towards differentiation at the expense of self-renewal.
393
394
395 **Discussion**
396 Here, we provided evidence that age-related increases in matrix stiffness compromise MuSC self-
397 renewal through stimulation of RNA decay, and that these effects can be reverted by exposing
398 old MuSCs to a soft matrix. We showed that aged muscle is approximately 3.5-fold stiffer than
399 young muscle, alterations we found to be associated with aberrant nuclear morphologies in old
400 MuSCs. Using substrates engineered to mimic the biophysical properties of young versus aged
401 muscle, we next found that aging affected the sensitivity of MuSCs to extrinsic biophysical signals.
402 That is, whereas an increase in matrix stiffness had little effects on the phenotype of young
403 MuSCs, old MuSCs exposed to a young-like matrix displayed a more youthful phenotype, as
404 evidenced by an increased number of old cells in the cycling and activated state (i.e., self-
405 renewing cells). When we compared static versus dynamic analyses of single cell lineage
406 trajectories, we found that dynamic assessments using RNA velocity captured the beneficial effect

407 of soft matrices on old MuSC responses. Specifically, a soft matrix reduced RNA degradation and
408 the stress response in old MuSCs, resulting in the promotion of a self-renewing subpopulation.
409 Our results highlight previously unrecognized mechanisms of old MuSC self-renewal in response
410 to extrinsic biophysical cues, while also suggesting rejuvenation of the cellular milieu as a strategy
411 to restore youthful fate transitions in old MuSCs.
412
413 The role of matrix stiffness on old MuSC fate has been investigated in the context of both
414 differentiating and self-renewing MuSCs. We and others have demonstrated the numerous
415 alternative fates old MuSCs adopt when exposed to age-related matrix stiffness, evidenced by
416 fibrogenic, inflammatory, and senescent conversions, ultimately contributing to hampered
417 myofiber repair in aged skeletal muscle (2, 8, 55, 56). Reports investigating the effects of stiffness
418 on old MuSC self-renewal, however, are fewer in number. Cosgrove et al. demonstrated
419 enhanced self-renewal of old MuSCs through exposure to p38 MAPK pathway inhibition
420 combined with culture on soft hydrogels (57). Similarly, our computational analyses identified that
421 aged matrices stimulated stress activated MAPK signaling, which corresponded with a loss of
422 self-renewing potential in old MuSCs. While aging was not studied directly, Moyle et al. recently
423 showed that matrix stiffness synergizes ligands essential for self-renewal, and further went on to
424 postulate that age-related stiffness may directly contribute to lost regenerative capacities with age
425 (58). However, mechanisms as to how aged matrices and kinase signaling disrupt the ability of
426 old MuSCs to self-renew have remained unclear. Our current work demonstrates that aged
427 matrices stimulate cell stress pathway activation and subsequently RNA decay to degrade the
428 transcripts essential for self-renewal, driving old MuSCs towards differentiation.
429
430 The relationship between RNA degradation and cellular fate transitions has been documented in
431 rodents (59-63), fruit flies (64), flatworms (65), and humans (66-68), spanning embryonic (66-68)
432 and adult stem cells (63, 68). The post-transcriptional control of MuSC fate has also been reported
433 (59, 60, 63, 69). Matrix stiffness is a well-documented morphogen that dictates fate transitions in
434 many cell types (5, 8, 70-72), including MuSCs (5, 8), and the results from our current studies
435 implicate a previously unestablished link between matrix stiffness and RNA decay in MuSCs that
436 contributes to age-related alterations in lineage specification.
437
438 Increased matrix stiffening, a quintessential feature of aged tissues and regarded by some as a
439 hallmark of aging (73), can in many ways be considered a form of cellular stress. Like many forms
440 of stimuli in cell signaling, a “sweet spot” exists, in that too much or too little stress causes, at

441 best, enhanced cellular resilience (74), and at worst, pathogenic outcomes such as cell death
442 (75). As matrix stiffness is a primary driver of mechanotransductive signaling, when increased
443 matrix stiffness of aged tissues falls outside a range of beneficial signaling, it is instead received
444 by the cell as a form of pathogenic stress. Cells respond to stress through evolutionarily conserved
445 surveillance mechanisms, which reorient both transcriptional and translational processes with the
446 goal of re-establishing homeostasis (76). Remodeling is achieved, at least in part, by stalling
447 protein synthesis and degrading transcripts related to the source of stress (77, 78). For example,
448 during endoplasmic reticulum (ER) stress and the unfolded protein response (UPR), not only is
449 protein synthesis halted as a result of the stress response, but the NMD pathway is also activated
450 to degrade already transcribed mRNAs in order to rapidly terminate the UPR (79). In terms of
451 matrix stiffness, it has recently been shown that pathological stiffness initiates DNA damage and
452 activates the DNA damage repair pathway (DDR) (80). Upon activation of the DDR, both ribosome
453 stalling and activation of the NMD pathway are initiated (81, 82) to clear repair response-related
454 mRNAs and terminate the DDR. In our studies, we identified Elk1-mediated ternary complex
455 formation, translational silencing, and NMD activation as primary drivers of the differential
456 responses of old MuSCs when seeded onto stiff versus soft matrices. Considering Elk1 is a stress-
457 activated MAPK (45) coupled with numerous studies demonstrating aberrant MAPK signaling in
458 old MuSCs (48, 83, 84), our results suggest that the inability to respond to stress in old MuSCs
459 contributes to an impaired self-renewing state. Future studies directly investigating the role of
460 NMD during stress and stem cell fate transitions, particularly through the lens of aging stem cells,
461 may yield intriguing insights into the loss of potency in old MuSCs.
462
463 To better understand the role of NMD in the sensitivity of old MuSCs to substrates of varying
464 stiffness, we performed *in silico* manipulation of *LSM14a*. LSM14a is a structural protein
465 necessary for processing body (P-body) formation, a cytoplasmic storage site for mRNA
466 degradation and, reported recently, a gatekeeper for cell fate transitions (68, 85, 86). In human
467 embryonic stem cells as well as adult progenitors (including myoblasts), P-body ablation resulted
468 in release of mRNAs encoding for pluripotent-specific transcription factors which, when translated,
469 induced a hyper-pluripotent state (68). While the impact of aging on P-bodies was not investigated
470 in this study, the predominance of biological processes associated with NMD in stem cells,
471 together with the role of LSM14a observed in our studies, suggests that changes in P-body
472 dynamics with age may impair the ability of MuSCs to self-renew upon division. Moreover, these
473 data further suggest that age-related matrix stiffness may impact P-body dynamics, potentially
474 influencing the lineage specification of old MuSCs. The potential interaction of P-body dynamics

and mechanical signals from the stem cell microenvironment is currently an unexplored area of research. Further research on these topics, as well as whether and how these mechanisms can be extrapolated to other adult progenitors in aged individuals, is needed.

The finding that young MuSCs maintain pluripotency regardless of substrate condition, while old MuSC lineage trajectories are readily manipulated by soft substrates is consistent with observations of a youthful resilience in the face of perturbation that is lost with increasing age (1). Over thirty years ago, principles of nonlinear dynamics and chaos theory were first used to describe the loss of complexity with aging that contributes to an inability of aged systems to respond to stress (87). It was postulated that young systems, spanning molecular to organismal scales, maintain vitality through a combination of highly complex and finely tuned biological processes that are required to efficiently respond to stress and maintain homeostasis. With aging, the loss of complexity underlies the inability of a system to respond to physiologic stress, causing functional breakdown. An example of these concepts at the organ level is seen in heart rate (HR) variability with aging. HR variability is highly irregular in young individuals, but variability drops considerably in old individuals (87). This loss of variability (i.e., complexity) renders older adults less able to adapt to stress, which associates with an increased likelihood of cardiac pathology. Similarly, in our study, young MuSCs were robust to perturbation even in the face of an aged matrix, showing minimal change in transcriptomic and phenotypic metrics. In contrast, the low transcriptional complexity of old MuSCs (i.e., impaired regulatory mechanisms) is evidenced by an inability to maintain self-renewal when challenged with the stress of a stiff matrix. The consequence of low complexity is evidenced by increasing rates of clonal drift in aging stem cell compartments, including both hematopoietic stem cells (88) and MuSCs (89). Importantly, we found that the consequence of low resilience in old MuSCs was mitigated when the source of stress (i.e., aged matrix stiffness) was minimized, as evidenced by an increased self-renewing potential. Just as nonlinear system approaches were required to describe the irregularity of aged heart rate variability, only *dynamo* RNA velocity vector fields, also derived from nonlinear mathematical approaches, effectively captured the transcriptional dynamics governing cell fate (41). Collectively, our results implicate old MuSC self-renewal as a system that is subject to a loss of complexity, and that aged matrix stiffness is a source of cellular stress.

509 **Limitations of Study**

510 There are limitations of the current findings worth noting. First, only two age groups were studied,
511 young and old, thereby limiting a holistic understanding of how the principles identified here
512 applies to the process of aging over the lifespan. Recent work from our group and others have
513 shown that aging is a non-linear process (90, 91), and additional ages will likely provide novel
514 insights into whether there is a tipping point at which MuSC display altered sensitivity to extrinsic
515 matrix cues, or if the decline is gradual and progressive (90). Second, only male mice were used.
516 Future studies are needed to compare the trajectory of stem cell fate changes over time and
517 according to sex. Third and finally, while our understanding of post-transcriptional control over
518 cellular function is growing rapidly, most research in this area is limited by snapshot-based
519 measurements. Recent reports have shown large fractions of the transcriptome never undergo
520 translation, thereby confounding our understanding of the relationship between gene expression
521 and protein production (92, 93). For instance, single cell metabolic labeling of nascent RNA
522 followed by fractionization of subcellular compartments revealed that only a subset of transcribed
523 RNAs get exported from the nucleus, while a large fraction gets degraded (93). Moreover, while
524 the importance of spatial information has gained increased appreciation since the advent of
525 spatial scRNA-seq, recent studies have shown a spatial distribution of the transcriptome and the
526 pronounced effect on rates of protein production, for which current sequencing technologies do
527 not account (92, 94). These limitations represent interesting opportunities for future investigation.
528
529
530
531
532
533
534
535
536
537
538
539
540
541

Acknowledgements: The authors thank Samuel K. Luketich and Drake D. Pedersen for their help with biaxial mechanical testing and Philip R. LeDuc for guidance with PDMS fabrication. All figures were prepared using Biorender. Data preprocessing and analysis were performed using Partek Flow Genomics Suite.

Funding: The study was supported by NIA R01 AG061005 (FA), NIA R01 AG052978 (FA), NIEHS R01 ES025529 (FA), NIDDK R01 DK119232 (JX), and NSF 2205148 (JX). Postdoctoral fellowship funding provided by P30AG024827 (ZH).

Author Contributions: Author contributions were determined using the CRediT model: Conceptualization: ZH, SH, HM, HI, AS, KW, GG, DV, TR, FA. Methodology: ZH, SH, HM, HI, AS, GG, AM, GN, AD. Investigation: ZH, SH, HM, HI, AS, AM, GN, AD. Visualization: ZH, SH, JX, FA. Funding acquisition: JX, FA. Project administration: FA. Supervision: JX, FA. Writing – original draft: ZH, FA. Writing – review & editing: ZH, SH, HI, AS, KW, GG TR, JX, FA.

Conflicts of Interest: The authors do not report any conflicts of interest**.**

576 **Figures:**

577 **Figure 1.**

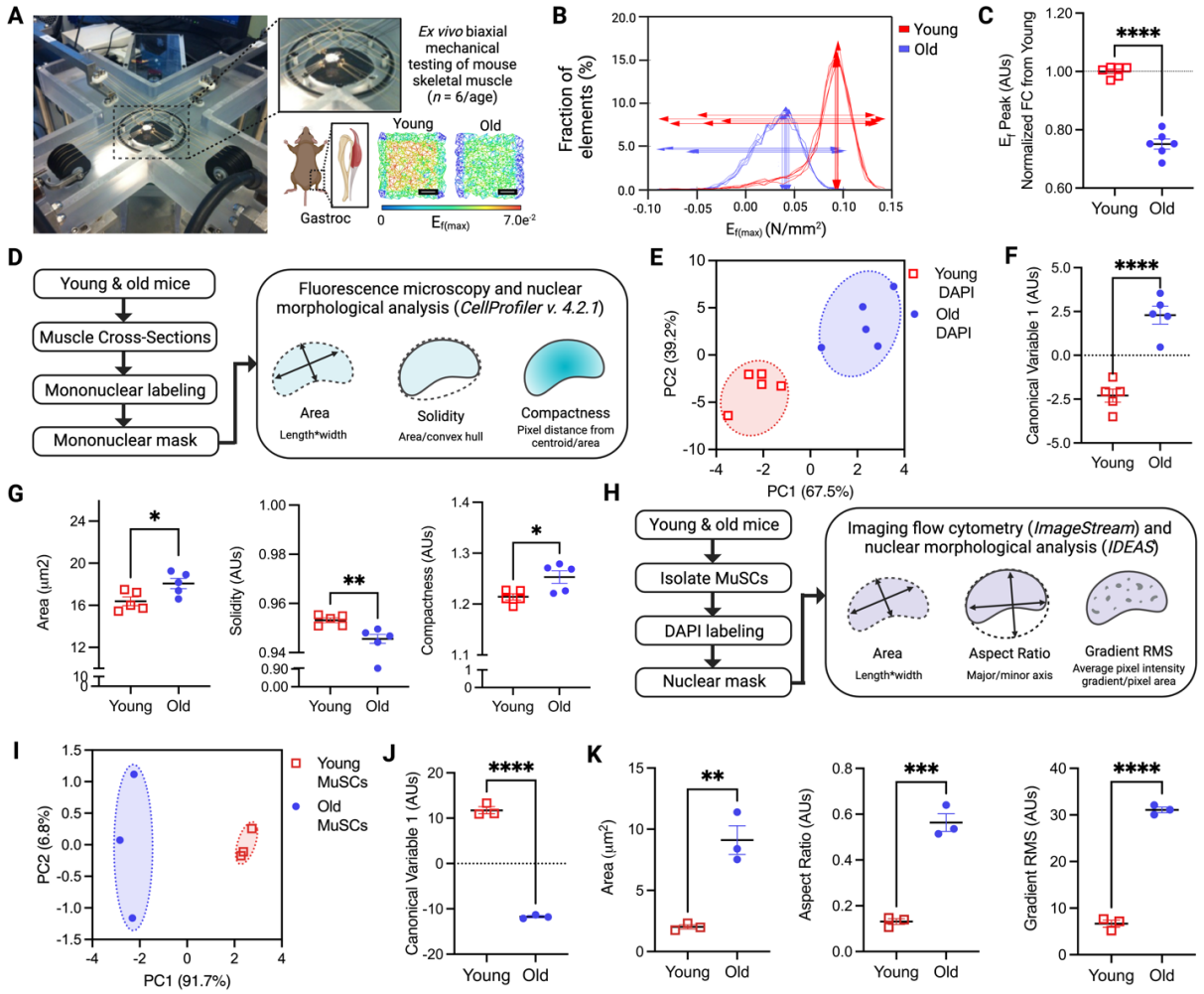

578

579

580

581

582

583

584

585

586

587

588

589

590 **Figure 2.**

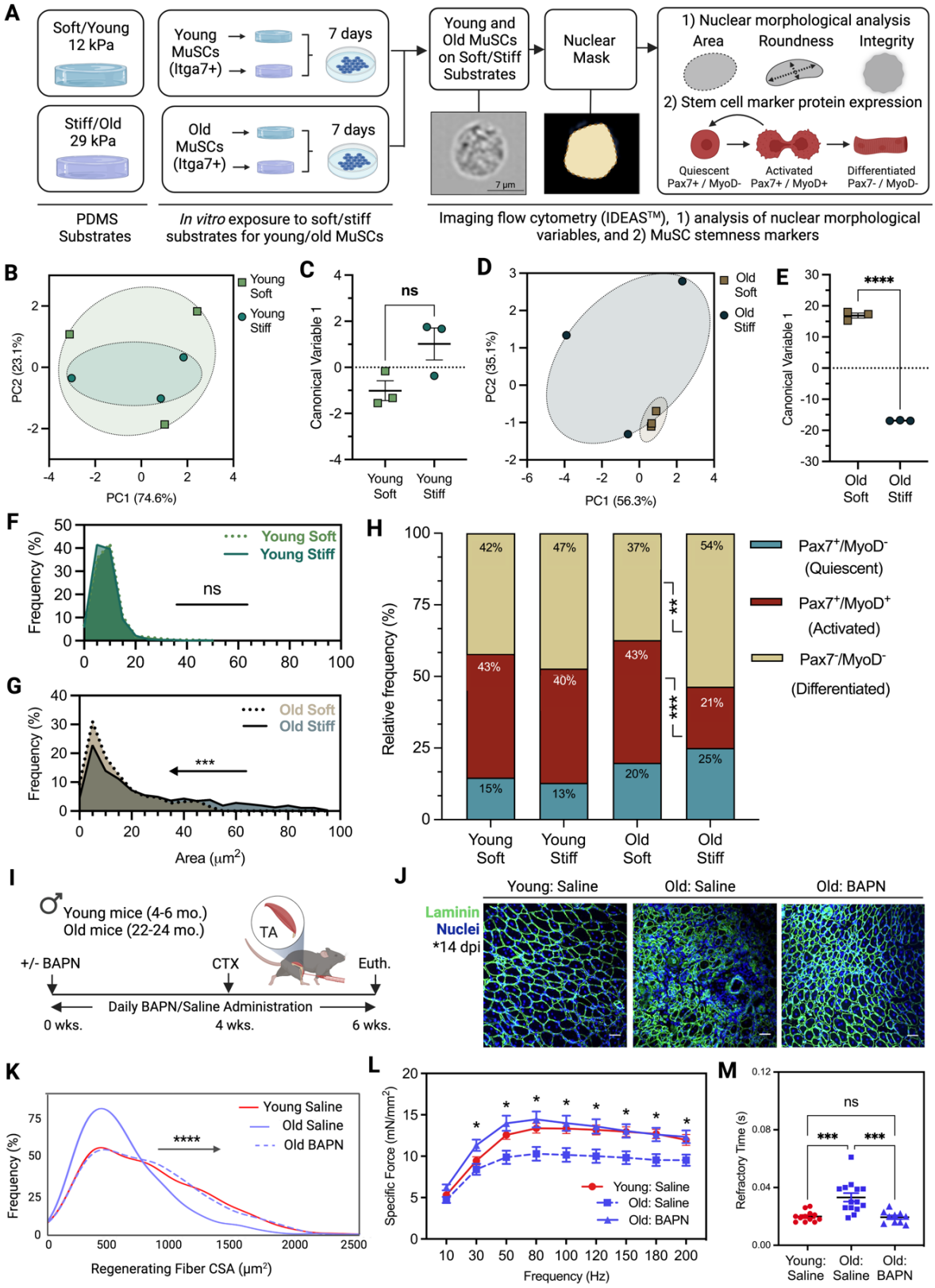

591

592 **Figure 3.**

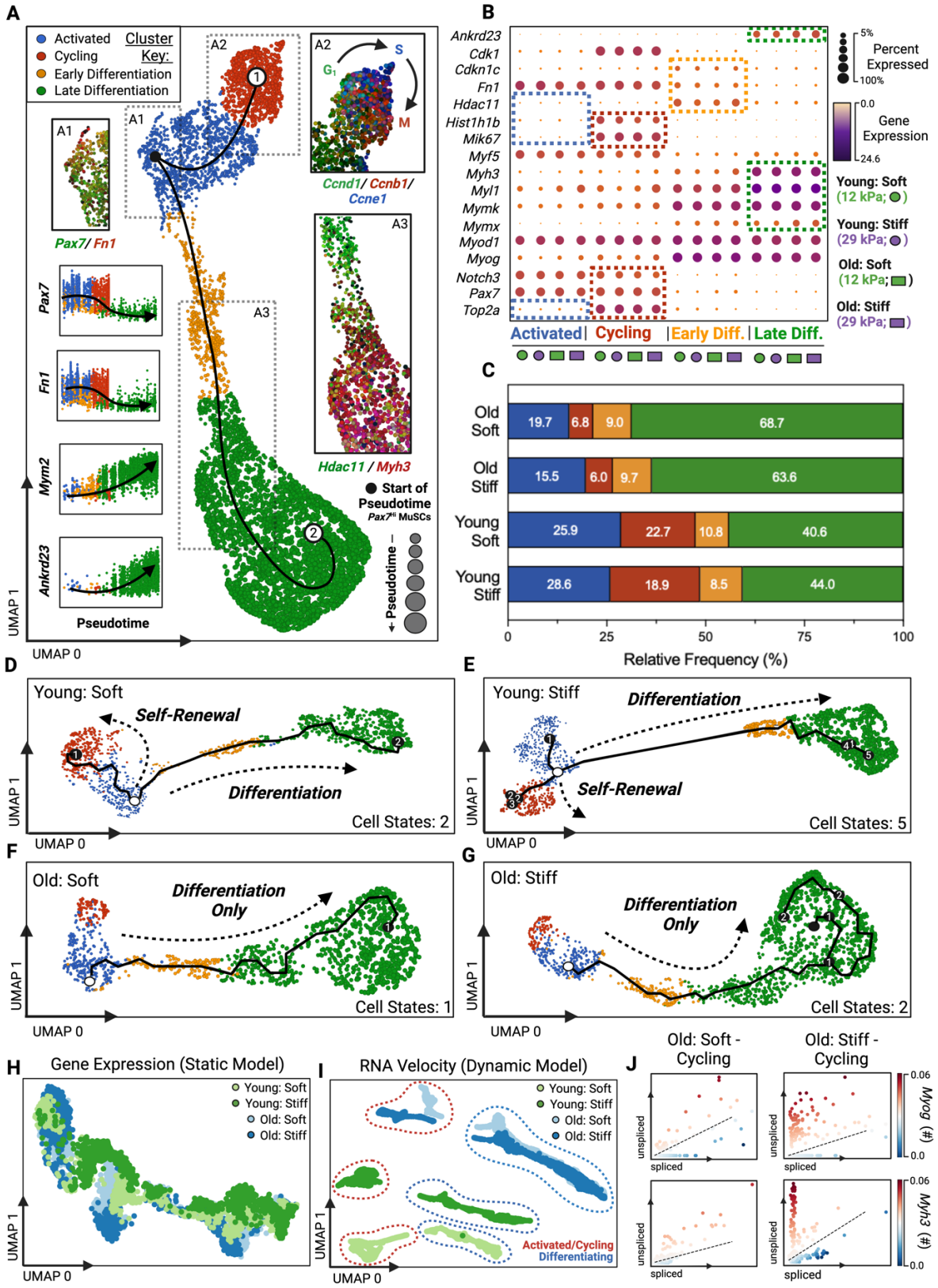

593

Figure 4.

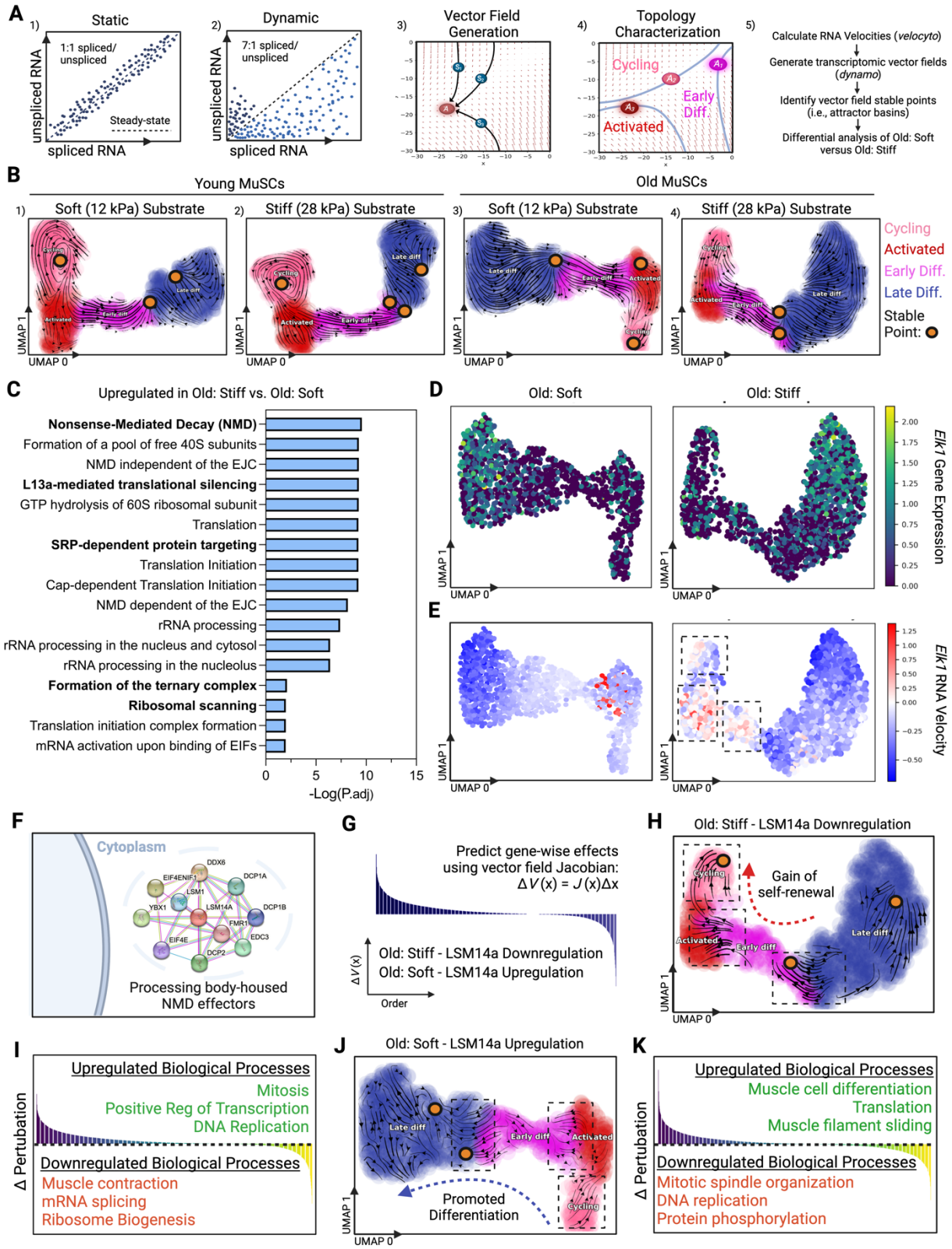
A
1) Static
1:1 spliced/ unspliced
Steady-state
unspliced RNA
spliced RNA
2) Dynamic
7:1 spliced/ unspliced
unspliced RNA
spliced RNA
3) Vector Field Generation
4) Topology Characterization
Cycling
Early Diff.
Activated
5)
Calculate RNA Velocities (velocyto)
Generate transcriptomic vector fields (dynamo)
Identify vector field stable points (i.e., attractor basins)
Differential analysis of Old: Soft versus Old: Stiff
B
Young MuSCs
Old MuSCs
1) Soft (12 kPa) Substrate
2) Stiff (28 kPa) Substrate
3) Soft (12 kPa) Substrate
4) Stiff (28 kPa) Substrate
Cycling
Activated
Early Diff.
Late Diff.
Stable Point:
UMAP 1
UMAP 0
C
Upregulated in Old: Stiff vs. Old: Soft
Nonsense-Mediated Decay (NMD)
Formation of a pool of free 40S subunits
NMD independent of the EJC
L13a-mediated translational silencing
GTP hydrolysis of 60S ribosomal subunit
Translation
SRP-dependent protein targeting
Translation Initiation
Cap-dependent Translation Initiation
NMD dependent of the EJC
rRNA processing
rRNA processing in the nucleus and cytosol
rRNA processing in the nucleolus
Formation of the ternary complex
Ribosomal scanning
Translation initiation complex formation
mRNA activation upon binding of EIFs
0
5
10
15
-Log(P.adj)
D
Old: Soft
Old: Stiff
Elk1 Gene Expression
E
Elk1 RNA Velocity
F
Cytoplasm
DDX6
EIF4ENIF1
DCP1A
LSM1
YBX1
LSM14A
DCP1B
FMR1
EIF4E
EDC3
DCP2
Processing body-housed NMD effectors
G
Predict gene-wise effects using vector field Jacobian:
ΔV(x) = J(x)Δx
Old: Stiff - LSM14a Downregulation
Old: Soft - LSM14a Upregulation
ΔV(x)
Order
H
Old: Stiff - LSM14a Downregulation
Gain of self-renewal
Cycling
Activated
Early diff
Late diff
I
Upregulated Biological Processes
Mitosis
Positive Reg of Transcription
DNA Replication
Downregulated Biological Processes
Muscle contraction
mRNA splicing
Ribosome Biogenesis
Δ Pertubation
J
Old: Soft - LSM14a Upregulation
Late diff
Early diff
Activated
Cycling
Promoted Differentiation
K
Upregulated Biological Processes
Muscle cell differentiation
Translation
Muscle filament sliding
Downregulated Biological Processes
Mitotic spindle organization
DNA replication
Protein phosphorylation
Δ Pertubation

597 **Figure Legends:**

598 **Figure 1. Age-related matrix stiffness is associated with aberrant MuSC nuclear**
599 **morphologies.** (**A**) Photograph of biaxial mechanical testing equipment. Representative
600 heatmaps of Green's strain energy map between young (4-6 months) and old (22-24) male mouse
601 gastrocnemius muscle. Scale: 50 µm. (**B**) Representative histogram depicting strain deformation
602 as a function of the fraction of elements obtained from mechanical testing (n=5/age). (**C**)
603 Quantification of $E_{f(max)}$ between young and old mouse muscle. (n=6/age). (**D**) Experimental
604 workflow of nuclear morphological analysis using CellProfiler. (**E**) PCA-LDA analysis and
605 quantification using nuclear morphological features between young and old muscle
606 mononucleated cells (n=6/age). (**F**) Quantification of LDA canonical variable 1. (**G**) Quantification
607 of nuclear area (μm^2), solidity (i.e., roundness), and compactness (i.e., nuclear integrity) of
608 mononucleated cells between young and old mouse muscle (n=5/age). (**H**) Experimental workflow
609 of imaging flow cytometry and nuclear morphological analysis. (**I**) PCA-LDA analysis and
610 quantification using nuclear morphological features between young and old MuSCs (n=3
611 mice/age group; 2,000 MuSCs represented per mouse). (**J**) Quantification of LDA canonical
612 variable 1. (**K**) Quantification of nuclear area (μm^2), aspect ratio (i.e., roundness), and gradient
613 RMS (i.e., texture/granularity) of mononucleated cells between young and old muscle (n=3
614 mice/age group; 2,000 MuSCs represented per mouse). Unpaired student T-tests were used for
615 Fig. C, F, G, J, K. Data are represented as mean ± SEM. *p<0.05; **p<0.01; ***p<0.001;
616 ****p<0.0001.

617

618 **Figure 2**. **Reducing matrix stiffness restores a more youthful cell state to old MuSCs**. (**A**)
619 Experimental design of PDMS fabrication, MuSC culture, and ISX analyses. (**B, C**) PCA-LDA
620 analysis and quantification using nuclear morphological features between young MuSCs cultured
621 on either soft or stiff substrates (n=3 mice/age group; 2,000 MuSCs represented per mouse). (**D,**
622 **E**) PCA-LDA analysis and quantification using nuclear morphological features between young
623 MuSCs cultured on either soft or stiff substrates (n=3 mice/age group; 2,000 MuSCs represented
624 per mouse). (**F**) Relative frequency of young MuSC nuclear area (μm^2) on either soft or stiff
625 substrates. (**G**) Relative frequency of old MuSC nuclear area (μm^2) on either soft or stiff
626 substrates. (**H**) Relative frequency of MuSCs with positive fluorescent signals for Pax7 and MyoD
627 between young and old MuSCs cultured on either soft or stiff substrates. Pax7+/MyoD-: quiescent,
628 Pax7+/MyoD+: Activated, Cycling, Pax7-/MyoD-: Differentiated. (**I**) Experimental design of β-
629 aminopropionitrile (BAPN) injections for preconditioning of skeletal muscle prior to injury between
630 BAPN and saline control injected mice (n=5-6 mice/group). (**J**) Representative images of muscle

631 cross sections immunolabeled with laminin (green) and DAPI (nuclei) between young mice
632 injected with control saline solution and old mice with either saline or BAPN injections. Scale bar:
633 200 μm^2 (**K**) Frequency distribution of regenerating muscle fiber area (μm^2) of TA muscle 14-days
634 post-injury (dpi) from BAPN and saline-treated old mice. (n=12-14 mice/group) (**L**) Force-
635 frequency curves from *in situ* contractile testing of recovering TA muscles 14 dpi between BAPN
636 and saline-treated old mice. (**M**) Half relaxation time from in situ contractile testing of recovering
637 TA muscles 14 dpi between BAPN and saline-treated old mice. Unpaired student T-tests were
638 used for Fig. C, E. Nonparametric Kolmogorov-Smirnov tests were used for Fig. F, G, K. ANOVAs
639 were used for Fig. H, L, M, followed by Tukey's post hoc when appropriate. Data are represented
640 as mean ± SEM. *p<0.05; **p<0.01; ***p<0.001; ****p<0.0001.
641
642 **Figure 3. Post-transcriptional dynamics contribute to stiffness-mediated lineage**
643 **specification.** (**A**) UMAP representation of aggregated MuSCs used for trajectory analysis from
644 young/old and soft/stiff conditions. Primary plot is colored based on stage of lineage progression
645 (Activated: blue, Cycling: red, Early Differentiation: green, Late Differentiation: orange).
646 Pseudotime and lineage progression is indicated by bubble size, increasing from Activated to
647 Cycling and Differentiated cell states. Expression of fibronectin (**A1**; *Pax7*/*Fn1*; activated), cyclin
648 D1 (**A2**; *Ccnd1*; cycling), cyclin B1 (**A2**; *Ccbn1*; cycling), cyclin E1 (**A2**; *Ccne1*; cycling), histone
649 deacetylase 11 (**A3**; *Hdac11*; early differentiation), and embryonic myosin heavy chain (**A3**; *Myh3*;
650 late differentiation) is provided via dotted insets for validation of cluster classification. Correlation
651 plots showing expression of *Pax7* (Activated, Cycling), *Fn1* (Activated, Cycling), *Mym2* (Early,
652 Late Differentiation), and *Ankrd23* (Early, Late Differentiation) changing as a function of
653 pseudotime is also provided. (**B**) Bubble plot indicating cluster-specific gene expression. Bubble
654 size corresponds to the percentage of cells within each subpopulation expressing the gene of
655 interest, and average expression value is indicated by heatmap. Dotted boxes indicate
656 subpopulation-specific gene expression (i.e., *Cdk1* is expressed only in the Cycling subpopulation
657 of MuSCs) (**C**) Relative frequency of MuSCs per lineage between young and old MuSCs on soft
658 and stiff matrices. (**D-G**) Lineage specification analysis using Monocle 3.0 for young and old
659 MuSCs exposed to soft and/or stiff substrates, each colored by subpopulation (Activated: blue,
660 Cycling: red, Early Differentiation: green, Late Differentiation: orange) . (**H**) Dimensionality
661 reduction method, UMAP, for visualization of the four samples using gene expression. (**I**) UMAP
662 for visualization of the four samples using RNA velocity. (**J**) Phase portraits of spliced-to-unspliced
663 gene counts for myogenin (*Myog*) and embryonic myosin heavy chain (*Myh3*) between old cycling
664 and activated MuSCs cultured on soft and stiff substrates.

Figure 4. Soft matrices reduce RNA decay pathway activity to preserve self-renewal in old MuSCs. (**A**) Schematic of transcriptional vector field generation and workflow. (**A1**) Example of a gene of interest (GOI) assumed to be in steady state when only mature gene counts are used. (**A2**) Example of a GOI in non-steady-state conditions, identified using the ratio of spliced to unspliced transcripts (i.e., RNA velocity). (**A3**) Example of a transcriptomic vector field generated using the RNA velocity values of each gene. (**A4**) Topology characterization of the vector field. Separatrices (blue lines) identify the boundaries of attractor basins ($A_{1\text{-}3}$) corresponding to each stable cellular state. (**A5**) Summary of experimental workflow using vector fields to identify how soft and stiff matrices influence self-renewal in old MuSCs. (**B**) Velocity vector fields depicting cellular fate progressions on UMAP space for young (**B1-2**) and old (**B3-4**) MuSCs on soft or stiff matrices. Coloring denotes stage of lineage progression. Stable fixed points indicate local stable phenotypes to which MuSCs are attracted. (**C)** Functional gene set enrichment of unique genes in rank-order identified using random forest classification between old MuSCs on soft and stiff matrices. Processes associated with the cellular stress response and RNA decay are highlighted via bolded text. (**D**) Comparison of *Elk-1* gene expression between old MuSCs on soft and stiff substrates. (**E**) Comparison of *Elk-1* RNA velocity between old MuSCs on soft and stiff substrates. Dotted boxes indicated elevated *Elk-1* RNA velocity in the cycling and activated states for old MuSCs on stiff matrices. (**F**) Schematic of physical interaction networks between processing body marker LSM14a mRNA processing body assembly factor (*LSM14a*) and NMD protein machinery. LSM14a physical interactions shown using STRING with interaction confidence set to high (0.7 out of 1.0). (**G**) Vector field perturbation scheme. (**H)** *In silico* perturbation of old MuSCs on stiff matrices of downregulated *LSM14a*. Cluster colors correspond to stage of lineage progression. Only significantly affected vectors are shown. (**I**) Gene set enrichment analyses of biological processes up and downregulated as a result of *LSM14a* downregulation in old MuSCs exposed to stiff matrices. (**J**) *In silico* perturbation of old MuSCs on soft matrices of upregulated *LSM14a*. Cluster colors correspond to stage of lineage progression. Only significant vectors are shown. (**K**) Gene set enrichment analyses of biological processes up and downregulated as a result of LSM14a upregulation in old MuSCs exposed to soft matrices. A Benjamini-Hochberg false discovery rate of 0.05 was used for multiple testing correction, and gene term size limits between 5-500 were used for gene set enrichment analyses (Fig. C, I, and K).

Supplemental Figures:

Figure S1.

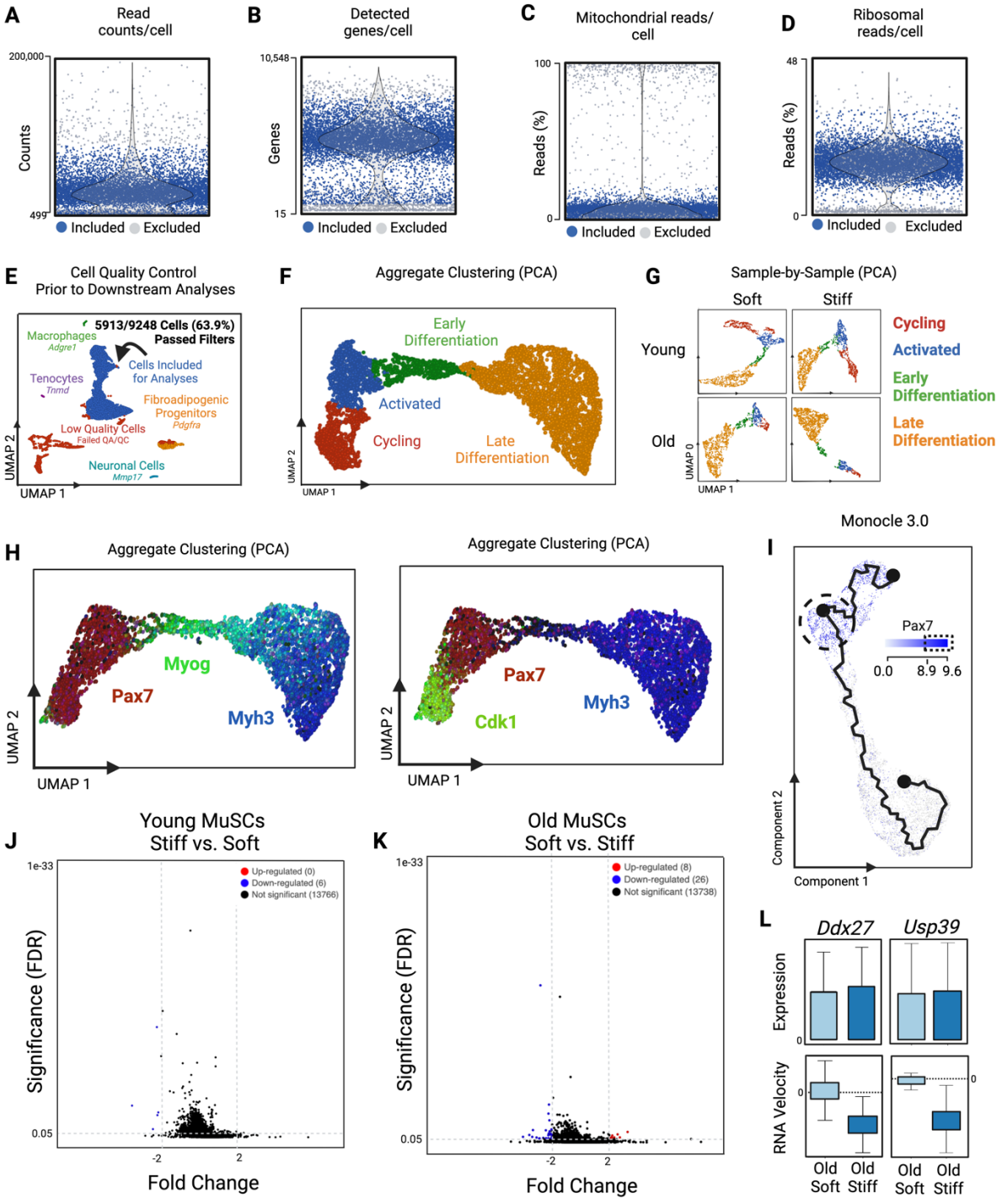

Figure S2.

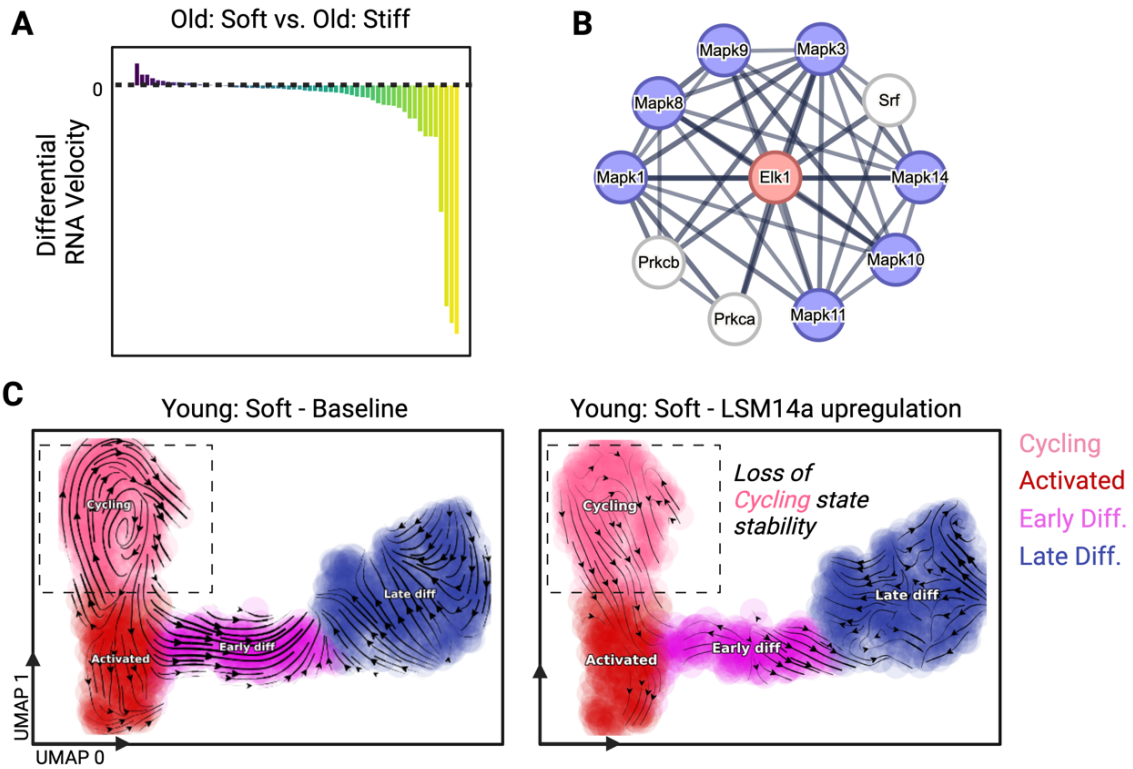
A
Old: Soft vs. Old: Stiff
0
Differential RNA Velocity
B
Mapk9
Mapk3
Mapk8
Srf
Mapk1
Elk1
Mapk14
Prkcb
Mapk10
Prkca
Mapk11
C
Young: Soft - Baseline
Young: Soft - LSM14a upregulation
Cycling
Activated
Early diff
Late diff
Loss of Cycling state stability
UMAP 1
UMAP 0
Cycling
Activated
Early Diff.
Late Diff.

Supplemental Figure Legends:

Figure S1. Single cell RNA sequencing data preprocessing of low-quality cells using metrics of: (**A**) read counts per cell, (**B**) detected genes per cell, (**C**) mitochondrial reads per cell, and (**D**) ribosomal read counts per cell. Grey colored cells outside the upper and lower quartiles of each metric were excluded while blue colored cells were included for analyses. (**E**) UMAP visualization of cells that passed quality control analyses but were computationally identified not to be a homogenous pool of MuSCs, likely from the small amount of error occurring from FACS sorting. Trace populations of fibro-adipose progenitor cells, macrophages, tenocytes, and neuronal cells were excluded to prevent confounders. (**F**) Dimensionality reduction using PCA projected onto UMAP space of all samples in aggregate. (**G**) Dimensionality reduction using PCA projected onto UMAP of each individual sample. (**H**) PCA-derived UMAP of demarcating genes used for cluster classification: *Pax7*, cyclin dependent kinase 1 (*Cdk1*), *Myog*, and *Myh3*. (**I**) UMAP projection of trajectory analysis colored by *Pax7*-Hi cells, representing the start of pseudotime progression. Volcano plot of differentially expressed genes between (**J**) young, and (**K**) old MuSCs on soft versus stiff matrices (-2>FC>2; p.adj<0.05). (**L**) Comparison of gene expression and RNA velocity of DEAD-box helicase 27 (*Ddx27*) and Ubiquitin Specific Peptidase 39 (*Usp39*) between old MuSCs on soft and stiff matrices.

Figure S2. (**A**) Random forest identification of differential RNA velocities between old MuSCs on soft versus stiff substrates. (**B**) Protein interaction network of ETS Like-1 protein Elk-1 (ELK1) using STRING. The confidence of interaction was set to high when determining ELK1 interactions (>0.9 out of 1.0). (**D**) *In silico* perturbation of vector fields projected onto UMAP of upregulated *LSM14a* in young MuSCs on soft matrices. Cluster colors correspond to stage of lineage progression. Only significant vectors are shown.

Supplemental File Legends:

Supplemental File 1. Gene sets from subclusters identified from aggregate UMAP clustering.

758 **STAR Methods:**

759 All reagents, equipment, and software code used are outlined in the **Key Resources Table** and
760 will be available upon publication.

761

762 **Resource Availability**

763 *Lead Contact*

764 Further information and requests for resources should be directed to and will be fulfilled by the
765 lead contact, Fabrisia Ambrosio (fambrosio@mgh.harvard.edu).

766

767 *Materials availability*

768 There were no new unique reagents used in this study.

769

770 *Data and code availability*

771 All data used to support the conclusions of this study are available from the corresponding author
772 upon reasonable request. This paper does not report original code. Information regarding
773 Monocle 3.0 (Monocle3 (RRID:SCR_018685), RNA velocity (RRID:SCR_018167), and *dynamo*
774 (RRID:SCR_017541), can be found using the SciCrunch Registry. The scRNA-seq data that
775 support the findings of this study will be available upon publication.

776

777 **Experimental model and subject details**

778 *Animals*

779 C57BL/6J young (4-6 months old) and aged (22-24 months old) male mice were received from
780 either the NIA rodent colony or Jackson Laboratories. All animal studies were approved by the
781 Institutional Animal Care and Use Committee of the University of Pittsburgh. Mice were housed
782 in pathogen-free cages with a temperature and humidity-controlled room with a 12-hour light/dark
783 cycle. Each cage received enrichment items, and food and water were provided *ad libitum*. On
784 average, 3-5 mice were housed per cage. The animals were assessed before the studies, and
785 any animals with obvious signs of health problems (e.g., lethargy, poor grooming, 20% weight
786 loss, or hunching) were excluded. All animals were then randomly assigned to intervention groups
787 and ear tagged. All investigators performing endpoint analyses were blinded to the experimental
788 group whenever possible.

789

790

791

792 *BAPN administration and cardiotoxin injuries*
793 Sterile saline or BAPN (290 μg/μl in sterile saline; approximately 550 μg/g of body weight;
794 CDS007521; Sigma, Burlington, MA, USA) was subcutaneously injected daily into the nape of the
795 neck of aged mice for a total of six weeks. Young mice received sterile saline injections alone for
796 the same timeframe to determine how aged BAPN injected mice compared to young. Four weeks
797 following the start of BAPN and/or saline injections, TA muscles were injured bilaterally via
798 intramuscular injection of cardiotoxin (10 μg/ml; 217503; Sigma). Two weeks following injury, TA
799 muscles were assessed for force producing capacity using in-situ contractile testing, and then
800 were immediately harvested, frozen, and stored at -80°C until further analysis.
801
802 *In situ contractile testing*
803 Contractile testing was performed 14 days after injury using an *in-situ* testing apparatus (Aurora
804 (Model 809B, Aurora Scientific Inc, Canada), stimulator (Model 701C, Aurora Scientific Inc), and
805 force transducer (Aurora Scientific Inc). Animals were anesthetized using 1.5-3% isoflurane prior
806 to the functional testing. The right Achilles tendon was cut, and the peroneal nerve was exposed
807 via a small incision on the right knee. Mice were then placed supine on a platform with the foot to
808 be tested positioned at 20° of plantarflexion and affixed to the footplate using cloth tape. The foot
809 was stimulated six times at a single frequency (60Hz) by placing a hook electrode on the peroneal
810 nerve. Half-relaxation time was quantified using the single twitch data. Next, successive tetanic
811 contractions at 10, 30, 50, 80, 100, 120, 150, 180, and 200 Hz were elicited to obtain a force-
812 frequency curve, with a 2-minute rest between contractions, as per our previous reports (90, 95).
813 Peak specific tetanic force was quantified by extracting the highest force value from the series of
814 tetanic contractions of each mouse. Animals displaying evidence of external injuries or tumor
815 growths were excluded from analysis. Functional testing was repeated by two independent
816 investigators over three cohorts of animals to ensure reproducibility.
817
818 **Method Details**
819 *Biaxial Testing*
820 Biaxial tensile testing of the gastrocnemius muscle was conducted as previously described (8).
821 Briefly, the medial head of the gastrocnemius muscle was collected from young and aged mice
822 and immediately placed in Ringer's solution for at least one hour before mechanical testing.
823 Muscle samples were cut into squares (5 mm x 5 mm) after measuring the sample thickness at
824 five individual points. Samples were then attached to a 50 g load cell with two loops of suture
825 connected to each side, with four hooks per side (see **Fig. 1A**). The sample deformation was

826 measured by real-time tracing of coordinates from a four-marker array positioned in the center of
827 each muscle sample. Gradient tensor F was calculated from the shape functions as previously
828 described(18). An equi-stress protocol was executed with the specimens submerged in PBS at
829 room temperature utilizing a tare load of 0.5 gram and a cycle time of 10 seconds each. Samples
830 were then tested up to the determined stress of 32 kPa, which was found to be the upper limit
831 muscles can tolerate without permanent deformation. All data were referenced to the pre-
832 conditioned float state.
833
834 *In-plane green's strain energy map*
835 A structural determinist approach was selected to quantify single fiber Green's strain (E) within
836 the gastrocnemius muscles tested under biaxial tensile states (96). First, fiber network models
837 were generated as stochastically equivalent to experimental samples based on the fibril network
838 architectural features previously evaluated using simple harmonic generation imaging (8). Fiber
839 intersection density, diameter, and orientation index were the input parameters of a mesh
840 generator. Artificial fiber networks were then matched with the distribution of fiber nodes,
841 orientation, and connectivity, and then extracted with digital image processing (18, 97). Taking
842 advantage of the biaxial test symmetry, square fiber network meshes were measured 500 μm by
843 500 μm to reduce the cost of the computational analysis (20). Biaxial tensile tests were then
844 simulated in Abaqus 6.14 (Dassault Systems, Waltham, MA), as described (20). Briefly, symmetry
845 boundary conditions were set on two edges of the square mesh, where axial displacements were
846 0, while axial loads from biaxial tests were applied on the remaining edges. All fibers were
847 computationally modelled with straight B22 beam elements, and the Yeoh hyper-elastic material
848 model was assigned (98). At the end of each analysis, results were automatically extracted with
849 a custom Python module to calibrate the Yeoh material parameters by fitting the experimental
850 biaxial data (98). After calibrating material properties, finite element analyses were run to evaluate
851 E_f maps and histograms under the biaxial tensile tests.
852
853 *Hydroxyproline assay*
854 The concentration of mature crosslinked and immature crosslinked and non-crosslinked collagen
855 was determined using previously established protocols (99). Briefly, freshly harvested TA muscles
856 from saline and/or BAPN treated mice were weighed, snap-frozen, and pulverized with a mortar
857 and pestle over dry ice. The samples were then rinsed in 1 mL of PBS with agitation for 30 minutes
858 at 4°C, and then centrifuged at 16,000g for 30 minutes at 4°C. Following centrifugation, PBS was
859 replaced with a 1:6 (weight: volume) solution of 0.5 M acetic acid (984303; Thermo Fisher,

860 Waltham, MA, USA) with 1 mg/ml pepsin (20343; Thermo Fisher) and stirred overnight at 4°C.
861 The following day, the samples were then centrifuged at 16,000g for 30 min at 4°C. Next, the
862 supernatant was collected as the pepsin-soluble fraction (PSF), or non-cross-linked and immature
863 crosslinked collagen, and the pellet was kept as the pepsin-insoluble fraction (PIF), or mature
864 crosslinked collagen. A 1:1 volume of 4 M NaCl was added to the PSF and incubated with
865 agitation for 30 minutes at 4°C before 30 minutes of centrifugation at 16,000g at 4°C. The
866 supernatant was then discarded, and the collagen fractions were measured using a
867 Hydroxyproline Assay Kit (ab222941; Abcam, Cambridge, UK) per the manufacturer's
868 instructions.
869
870 *Analysis of muscle regeneration*
871 Muscle tissues were frozen by completely immersing in liquid nitrogen-cooled 2-Methylbutane for
872 1 minute. Frozen muscles were sectioned at 10 µm thickness using CryoStar NX50 Cryostat
873 (Thermo Fisher,). Muscle sections were then fixed in 2% paraformaldehyde solution (J19943K2,
874 Thermo Fisher) diluted in PBS followed by three 5-minute PBS washes at room temperature.
875 Samples were permeabilized with 0.01% Triton X-100 in PBS for 15 minutes and blocked with
876 3% bovine serum albumin (A7906, Sigma) in 0.01% Triton X-100 in PBS (blocking buffer) for 1
877 hour at room temperature. The sample slides were incubated with rat anti-Laminin (ab79057,
878 Abcam, Cambridge, UK) in 5% goat serum (191356, MP Biomedicals, Solon, OH) in blocking
879 buffer overnight at 4 °C. The slides were washed for 5 minutes 3 times with PBS followed by
880 incubation with goat anti-Rat IgG (H+L) Alexa Fluor 594 secondary antibody (A11012, Thermo
881 Fisher) at 1:500 dilution for one hour at room temperature. After three 5-minute PBS washes, the
882 samples were incubated with 4',6-diamidino-2-phenylindole (DAPI) (422801, BioLegend, San
883 Diego, CA) for 2 minutes at room temperature. The slides were washed once with PBS for 5
884 minutes before coverslips (12-545-100, Thermo Fisher) were mounted with Gelvatol mounting
885 media (81365; Sigma) and let to dry. Images were taken using inverted microscopy (Observer
886 Z1, Carl Zeiss AG, Oberkochen, Germany) with a 20x objective lens. The area of centrally
887 nucleated myofibers was measured using ImageJ software using a previously established
888 protocol (100).
889
890 *Primary muscle stem cell (MuSC) isolation and culture*
891 MuSCs were freshly isolated from young/aged mice for each experiment using previously
892 established protocols (101). Briefly, forelimb and hindlimb musculature were dissected and placed
893 in ice cold wash media (Hanks Balanced Saline Solution (HBSS); Thermo Fisher, 10% Fetal

894 Bovine Serum (FBS); Thermo Fisher, 1% Penicillin-Streptomycin; Thermo Fisher). Muscles were
895 then finely chopped and then incubated with agitation in 750 U/mL of Collagenase II (Gibco) for
896 one hour, followed by an additional 30 minutes in 1000 U/mL Collagenase II and 100 U/mL
897 Dispase (Gibco). Mononuclear cells were then collected through a 40 μm strainer (Thermo
898 Fisher), and immunolabeled with antibodies for CD31, CD45, Sca1, and Integrin α7, as previously
899 described (11-0311-82; 11-0451-82; 25-5981-82; MA5-23555, respectively; Thermo Fisher)
900 (101). Propidium iodide was used as a dead cell marker (1mg/ml aqueous solution; 25535-16-4,
901 Alfa Aesar, Lancashire, UK). Cells were then sorted using fluorescence-activated cell sorting (BD
902 Biosciences; Franklin Lakes, New Jersey, USA) based on live/dead and negative expression of
903 CD31, CD45, and Sca1.
904
905 *Quantification of nuclear morphology*
906 For the quantification of nuclear morphology, DAPI-labeled cross sections and isolated MuSCs
907 were obtained at 40x magnification using an A1 confocal microscope (Nikon, Tokyo, Japan).
908 Afterwards, image processing and morphometric feature extraction were performed using
909 CellProfiler™ software (v4.0, The Broad Institute). Fifty-three shape features of nuclei were
910 determined using the "identify primary objects" followed by the "measure object size shape" and
911 "export to spread sheet" module. Principal Component Analysis (PCA; unsupervised) and PCA-
912 linear discriminant analysis (PCA-LDA; supervised) were performed to facilitate the identification
913 of segregation of the nuclear morphological features identified by CellProfiler™ software (23). In
914 PCA-LDA analysis, the small number of PCs corresponds to sample size in each group, were
915 included to prevent overfitting. To determine variables of nuclear shape contributing to PCs,
916 loading matrix, a correlation between the original variable and PCs, were extracted.
917
918 *PDMS fabrication*
919 PDMS substrates with different stiffnesses were prepared as previously described. Briefly,
920 Sylgard 527 was prepared by mixing 1) equal weights or 2) 1:1.8 weight ratio of Dielectric Gel
921 Part A and Part B and mixed well manually for 12 kPa and 29 kPa substrates, respectively
922 (NC1208196; Thermo Fisher). The mixtures were degassed using a vacuum desiccator for 30
923 minutes. Next, PDMS was poured into 60 mm diameter Petri dishes to make ~1.2 mm thick
924 substrate for cell culture. Alternatively, 30 μL of PDMS was poured onto an 18 mm circular
925 coverslip followed by a one-minute spin at 930 rpm using a spin coater (Laurell WS-650SZ-
926 6NPP/A1/AR1) to make ~ 100 μm-thick films for cell culture for immunocytochemistry imaging of
927 cell on PDMS substrates. PDMS substrates were cured at 60 °C for 16 hours for all experiments.

928 PDMS substrates were treated with plasma cleaner (Harrick Plasma, Ithaca, NY) at the medium
929 power setting for 20 seconds and soaked in water until the next step. Water was replaced with
930 70% ethanol and sterilized for 30 minutes under UV light in a cell culture hood. PDMS substrates
931 were rinsed with sterile water three times and coated with 50 µg/mL of fibronectin (F4759, Sigma-
932 Aldrich, St. Louis, MO) diluted in water for one hour at room temperature. Fibronectin solution
933 was then removed, and the substrates were rinsed with water twice, followed by a PBS rinse
934 before cell seeding. PDMS substrates were never left dry after plasma treatment. Cells were
935 seeded on PDMS substrates at ~ 160 – 200 cells/mm^2.
936
937 *Immunofluorescence and image acquisition*
938 For the nuclear morphology image analysis, freshly isolated young MuSCs were cultured on soft
939 or stiff PDMS substrates for a week before nuclear staining and imaging of the cells on the PDMS
940 substrates to avoid potential alterations in cell morphology by transfer of the cells. For the staining
941 of other experiments for morphological analysis of adherent cells, MuSCs were fixed and stained
942 with DAPI two days after seeding, which is just enough time to allow MuSC adhesion to the
943 substrate. The following antibodies were used for the other immunostaining studies: Mouse anti-
944 PAX7 antibody at 5 µg/mL (DSHB, Iowa, U.S.A.) and Rabbit anti-MyoD antibody at 1:500 (sc-
945 760, Santa Cruz, Texas, U.S.A.).
946
947 *Imaging flow cytometry and analysis*
948 Isolated MuSCs were plated on soft/stiff substrates and cultured for seven days. Next, the cells
949 were trypsinized with 0.25% trypsin for one minute at 37°C and collected in 1.5 mL Eppendorf
950 tubes for subsequent analysis. The pelleted cells were fixed, permeabilized, blocked, and
951 immunolabeled for myogenic markers of Pax7 and MyoD. Labeled cells were imaged at single-
952 cell resolution using imaging flow cytometry (ISX; Flow cytometry core, Department of
953 Immunology, University of Pittsburgh). ISX was conducted using a 60X objective at a resolution
954 of 0.3 µm^2/pixel. Filtered sheath buffers were used to ensure the absence of debris and non-
955 cellular components. Samples were acquired using INSPIRE® software with the highest
956 sensitivity by acquiring images at the lowest speed. All lasers employed were used at the optimal
957 power settings based on an unstained cell control. Gating was performed on unstained control
958 cells for acquiring images of single and focused cells. For analyzing myogenic markers, IDEAS
959 software was used by performing a nuclear co-localization step to detect the true positives (i.e.,
960 Pax7 and MyoD fluorescent intensity) in the imaging dataset. Nuclear morphology features were
961 extracted using IDEAS software per cell, which were used for downstream computational

962 analysis. Every experiment was performed in at least two independent runs. In every run, three
963 sets of imaging data were acquired. Data were presented as an average of the three sets of
964 imaging data in one representative run.
965
966 *Single cell RNA sequencing*
967 Both young and old MuSCs were collected at the same timepoints after culturing on soft or stiff
968 surfaces for single cell RNA sequencing (scRNA-seq) to minimize batch effects (102). A total of
969 three mice per age group were used for cell isolations to ensure biological diversity, and a total of
970 three technical replicates per substrate condition were used to mitigate experimental error.
971 Following the collection of cells from PDMS experiments, MuSCs were loaded into a 10X
972 Chromium Controller using the Single Cell 3' Reagent kit v3 per manufacturer's instructions (10x
973 Genomics, Pleasanton, CA, USA). Resulting libraries were sequenced on an Illumina NovaSeq
974 6000 platform yielding a read depth of 200 million reads/sample (Novogene, China).
975
976 *Single cell RNA sequencing data preprocessing*
977 The Cell Ranger pipeline (6.1.2) was utilized to align each sample's reads to the mouse reference
978 genome (mm10). The unspliced and spliced counts for each sample were obtained using *velocyto*
979 (0.17.17). For downstream analysis, the gene filtering and normalization was performed using
980 *dynamo* (1.1.0, https://github.com/aristoteleo/dynamo-release) in python. For each sample, the
981 cells filtered out with the Monocle 3.0 preprocessing were also filtered out for *dynamo* downstream
982 analysis. Briefly, the filtration of gene counts and cells were based on the following criteria: genes
983 expressed in only 1.0% of total cells, cells expressing >20.0% of mitochondrial-related gene
984 counts, cells expressing <5% of ribosomal-related reads, and trace amounts of non-myogenic
985 cells (i.e., fibroadipo-progenitor cells (*Pdgfra*), macrophages (*Adgre1*) tenocytes (*Tnmd*), and
986 neuronal cells (*Mmp17*), For downstream analysis a total of 5,913 cells and 32,285 genes were
987 obtained from all samples. In the *dynamo* preprocessing step (recipe monocle), the top 4000
988 genes were utilized for RNA velocity calculation following size normalization and log1p
989 transformation. For visualization purposes, dimensionality reduction was performed with UMAP
990 on the 30-dimensional PCA space that was obtained from *dynamo*'s *reduceDimension* function.
991
992 *Dimensionality Reduction*
993 For gene expression, combining all cells from each sample and selecting the intersection of all
994 genes that were labeled as "use_for_dynamics" in *dynamo* results in a 5,913 cell by 1363 gene
995 expression matrix. With this, UMAP was performed. For RNA velocity, combining all cells from

each sample and selecting the intersection of all genes that were labeled as “use_for_dynamics” in *dynamo* results in a 5,913 cell by 1363 gene expression matrix. Extracting the RNA velocity for each gene for each cell results in a 5,913 cell by 1363 gene velocity matrix. With this, UMAP was performed.

Classifying cells

The classification of cells into the one of the four groups, cycling, activated, early differentiation, and late differentiation was obtained using a combination of unsupervised graph-based clustering as well as manual characterization using previously reported state-specific markers (2, 56, 103). Following dimensionality reduction using PCA and visualization using UMAP, the Louvain clustering algorithm was performed to generate clusters based on discrete cluster-specific gene expression. The corresponding gene sets were then used to 1) corroborate cluster annotation with previously published datasets and 2) to generate bubble plots indicating cluster-specific gene expression. Bubble plots were generated following cluster classification by determining the average expression of each gene of interest (GOI) per cluster, followed by measuring the percentage of cells within each cluster expressing each GOI.

Monocle 3.0

Trajectory analysis was performed using Monocle 3.0 using the same preprocessed data as used for *dynamo* analyses. Briefly, following preprocessing (see Preprocessing MuSC scRNA-seq data), dimensionality reduction was performed using UMAP. To confirm annotation of MuSC subclusters using Monocle 3.0 was the same as conventional dimensionality reduction approaches, the trajectory was probed for expression of genes corresponding to each cellular state (i.e., activated, cycling, early differentiation, and late differentiation). Following annotation, cells with the highest expression of *Pax7* were selected as the start point for pseudotime progression. Cells with high expression of Pax7 *in vivo* have been shown to represent MuSCs with the highest degree of pluripotency (104). Pseudotime progression in the aggregated dataset (i.e., inclusion of all four groups) corroborated our subcluster annotation by showing both self-renewing and differentiating trajectories. A correlation analysis of gene expression along pseudotime progression was performed to identify genes expressed throughout each trajectory, which are shown in Fig. 3A, as well as the bubble plot in Fig. 3B. Following aggregate trajectory characterization, individual trajectory analysis for each sample was performed.

1030 *Differential analysis*

1031 The gene specific analysis (GSA) feature of Partek Flow was used for differential analysis of gene
1032 expression between samples, which is equivalent to limma-trend (102) (Partek Genomics, St.
1033 Louis, MO, USA). The resulting gene sets were filtered using an FDR step up (p.adj) of 0.05.
1034 Genes +/- 2-fold change were determined to be statistically significant.

1035

1036 *RNA velocity*

1037 RNA velocity estimations were made using *dynamo*, as previously described (41). Briefly, reads
1038 were aligned to the mm10 mouse reference transcriptome with *cellranger,* and *velocyto* was
1039 utilized to quantify the read counts of both pre-mRNA (unspliced; mapped exon-intron boundaries,
1040 or the intron of the transcript alone) and mature mRNA (spliced; mapping only to exonic regions
1041 of transcripts). To remain consistent with the previous analysis performed with Monocle 3.0, cells
1042 filtered out in the Monocle 3.0 analysis were also filtered out for the *dynamo* analyses. The
1043 following set of ordinary differential equations model the turnover dynamics of a specific gene *i*
1044 that is actively transcribed in a cell,

1045 $$\frac{du_i}{dt} = \alpha_i - \beta_i u_i,$$

1046 $$\frac{ds_i}{dt} = \beta_i u_i - \gamma_i s_i,$$

1047 where u_i represents the number of unspliced RNA copies of gene *i*, $\frac{du_i}{dt}$ is the rate of production
1048 of unsliced transcripts, s_i represents the number of spliced RNA copies, $\frac{ds_i}{dt}$ is the rate at which
1049 spliced RNA copies are produced (i.e., RNA velocity), α_i is the rate of transcription, β_i is the rate
1050 constant of transcript splicing, and γ_i is the rate constant of transcript degradation. u_i and s_i were
1051 both measured in scRNA-seq. Furthermore, with $\tau_i = \beta_i t, \widetilde{\gamma_i} = \gamma_i/\beta,$ one can define a scaled RNA
1052 velocity of a gene relative to its own splicing time scale, $\frac{ds_i}{d\tau_i} = u_i - \widetilde{\gamma_i} s_i$. The scaled gene specific
1053 degradation rate constant $\widetilde{\gamma_i}$ was determined using Ordinary Least Squares regression as in the
1054 original RNA velocity paper of La Manno et al. (40), in which a pseudo steady state was assumed
1055 to lie in the *u-s* phase space where cells have extreme high unspliced and high spliced RNA
1056 expression.

1057

1058 *Continuous vector field reconstruction*

1059 Detailed methodology on vector field reconstruction has been published previously by Qui et al
1060 (41). In brief, *dynamo* aims to reconstruct a continuous vector field from discrete gene expression
1061 data obtained from scRNA-seq data and instantaneous RNA velocities. Notice that α is a function

of the concentrations of the elements regulating a gene under consideration, so a function of $\boldsymbol{s}$ under a Markovian assumption (105), and $\frac{d\boldsymbol{s}}{dt} = \boldsymbol{F}(\boldsymbol{s})$, where the vector $\boldsymbol{s}$ represents the gene expression, $\frac{ds}{dt}$ represents the RNA velocity, and $\boldsymbol{F}$ represents the learned vector field function, containing genome wide regulation, mapping any point in the gene expression space to the RNA velocity space.

Vector field differential geometry analysis

We projected the reconstructed continuous vector field onto a two-dimensional UMAP space, then identified fixed points that indicate the behavior and direction a cell at a specific cellular state tends to move along the transcriptional landscape. In other words, one can predict on the transition between cell states over an arbitrary time scale.

As before, the details of these calculations and derivations are available in the original *dynamo* publication (41). In brief, a fixed point is where the value of the vector field function is zero. The eigenvalues of the Jacobian of that point was evaluated to categorized that point as either a stable fixed point (attractor), unstable fixed point (repulsor), or a saddle point. From the Jacobian obtained from the vector field, one can characterize fixed points and observe where cells end up in the cell state space. With this, we can then ask the question "(1) did the cell reach a point in space where results in no changes in the cell state (i.e., stable), or (2) did the cell continue to change states in space indefinitely (i.e., unstable)?"

Random forests classification

Given the emergence of stable points in the cycling and activated cell states for old MuSCs on a soft substrate compared to stiff, each of these states were selected for differential analyses using random forest classification. To reduce the number of features, the intersection of all genes that were labeled as "use_for_dynamics" in *dynamo* were selected for a total of 1363 genes. With this set of cells and genes, the corresponding RNA velocities for each gene per each cell were utilized as the input data for the random forests. Ten rounds of random forests, using *sklearn*, were performed (n_estimators = 100, max_features = 'sqrt', max_depth = 1, class_weight = 'balanced') with a 0.8 and 0.2 training and testing data split, respectively. The max depth of 1 was chosen to extract the genes that displayed the greatest degree of differential velocities between groups. For each round of random forests, the important features were extracted.

Gene set enrichment and TRANSFAC analysis

Following gene set generation from either random forest classification or unique biomarkers per subcluster classification, genes were imported into gProfiler (https://biit.cs.ut.ee/gprofiler/) in rank-order. Prior to analysis, multiple testing was corrected for using a Benjamini-Hochberg false discovery rate of >0.05. To account for overlap in synonymous biological processes, a term size limit greater than 5 and less than 500 was selected (106). To identify predicted transcription factors common to nucleotide sequences of the inputted gene sets, TRANSFAC was used with similar testing correction parameters (47).

Protein-protein interaction networks

STRING (https://string-db.org/) was used to infer physical binding partners of LSM14a, as well as signaling partners of Elk1, as has been previously described. Briefly, each gene of interest (GOI) was input into the STRING database, and settings were made according to each GOI. For LSM14a, “physical subnetwork” and “high confidence” of interaction scores was selected, along with a maximum of no more than 20 interactions. For Elk1, “full STRING network”, “high confidence” of interactions, and no more than 10 interactions were selected for network generation.

Vector field in silico perturbations

The Jacobian can also be utilized to understand gene-gene regulations such as whether a gene upregulates or down regulates another gene. Mathematically, a Jacobian element $\frac{\partial F_i}{\partial s_j}$ encodes how the transcriptional velocity of gene i is impacted by changes in expression of gene j. Consider that the expression state of a cell changes form $\boldsymbol{s}$ to $\boldsymbol{s} + \Delta\boldsymbol{s}$ through, e.g., adding one or some of the transcripts ectopically by amount $\Delta\boldsymbol{s}$, then the vector field changes approximately to,

$$\boldsymbol{F}(\boldsymbol{s} + \Delta\boldsymbol{s}) \approx \boldsymbol{F}(\boldsymbol{s}) + \boldsymbol{J} \cdot \Delta\boldsymbol{s}.$$

Thus $\boldsymbol{J} \cdot \Delta\boldsymbol{s}$ propagates the genetic perturbation $\Delta\boldsymbol{s}$ through the gene regulatory network.

Quantification and statistical analysis

Statistics

Sample size determination for CellProfiler, ImageStream, and *in vivo* analyses were determined from our previously published studies (29, 90, 95). For experiments using isolated MuSCs requiring a power level of 0.08, n=3 mice/age were used. For *in vivo* experiments requiring an alpha level of 0.08, n=5/mice/age were used. For scRNA-seq experiments, isolated MuSCs from

n=3 mice/age were used for *in vitro* experiments, which were split into three technical replicates prior to sequencing. A read depth of 200 million reads/sample was collected to ensure adequate power (107). Statistical analyses were performed using GraphPad Prism (v. 9.0). Significance was assumed at an alpha level of 0.05. Kolmogorov-Smirnov test and F-test were initially performed to assess normality and equality of variance, respectively. For all ANOVA analyses resulting in a p-value of less than 0.05, appropriate post-hoc tests were performed and described in figure legends. For multiple comparisons, Bonferroni correction methods were performed to mitigate type I error inflation.

1162 **References:**

1163

1164 1. Blau HM, Cosgrove BD, and Ho AT. The central role of muscle stem cells in
1165 regenerative failure with aging. *Nat Med.* 2015;21(8):854-62.
1166 2. Kimmel JC, Hwang AB, Scaramozza A, Marshall WF, and Brack AS. Aging induces
1167 aberrant state transition kinetics in murine muscle stem cells. *Development.*
1168 2020;147(9).
1169 3. Wang J, Zhang K, Xu L, and Wang E. Quantifying the Waddington landscape and
1170 biological paths for development and differentiation. *Proceedings of the National*
1171 *Academy of Sciences.* 2011;108(20):8257-62.
1172 4. Goldberg AD, Allis CD, and Bernstein E. Epigenetics: a landscape takes shape. *Cell.*
1173 2007;128(4):635-8.
1174 5. Engler AJ, Sen S, Sweeney HL, and Discher DE. Matrix elasticity directs stem cell
1175 lineage specification. *Cell.* 2006;126(4):677-89.
1176 6. Gilbert PM, Havenstrite KL, Magnusson KE, Sacco A, Leonardi NA, Kraft P, et al.
1177 Substrate elasticity regulates skeletal muscle stem cell self-renewal in culture. *Science.*
1178 2010;329(5995):1078-81.
1179 7. Gosselin LE, Adams C, Cotter TA, McCormick RJ, and Thomas DP. Effect of exercise
1180 training on passive stiffness in locomotor skeletal muscle: role of extracellular matrix. *J*
1181 *Appl Physiol (1985).* 1998;85(3):1011-6.
1182 8. Stearns-Reider KM, D'Amore A, Beezhold K, Rothrauff B, Cavalli L, Wagner WR, et al.
1183 Aging of the skeletal muscle extracellular matrix drives a stem cell fibrogenic conversion.
1184 *Aging Cell.* 2017;16(3):518-28.
1185 9. Zimmerman SD, McCormick RJ, Vadlamudi RK, and Thomas DP. Age and training alter
1186 collagen characteristics in fast- and slow-twitch rat limb muscle. *J Appl Physiol (1985).*
1187 1993;75(4):1670-4.
1188 10. Freitas-Rodríguez S, Folgueras AR, and López-Otín C. The role of matrix
1189 metalloproteinases in aging: Tissue remodeling and beyond. *Biochim Biophys Acta Mol*
1190 *Cell Res.* 2017;1864(11 Pt A):2015-25.
1191 11. Lacraz G, Rouleau AJ, Couture V, Söllrald T, Drouin G, Veillette N, et al. Increased
1192 Stiffness in Aged Skeletal Muscle Impairs Muscle Progenitor Cell Proliferative Activity.
1193 *PLoS One.* 2015;10(8):e0136217.

1194 12. Wood LK, Kayupov E, Gumucio JP, Mendias CL, Claflin DR, and Brooks SV. Intrinsic
1195 stiffness of extracellular matrix increases with age in skeletal muscles of mice. *J Appl*
1196 *Physiol (1985).* 2014;117(4):363-9.
1197 13. Mann CJ, Perdiguero E, Kharraz Y, Aguilar S, Pessina P, Serrano AL, et al. Aberrant
1198 repair and fibrosis development in skeletal muscle. *Skeletal Muscle.* 2011;1:21-.
1199 14. Rosant C, Nagel MD, and Pérot C. Aging affects passive stiffness and spindle function
1200 of the rat soleus muscle. *Exp Gerontol.* 2007;42(4):301-8.
1201 15. Gao Y, Kostrominova TY, Faulkner JA, and Wineman AS. Age-related changes in the
1202 mechanical properties of the epimysium in skeletal muscles of rats. *J Biomech.*
1203 2008;41(2):465-9.
1204 16. Schüler SC, Kirkpatrick JM, Schmidt M, Santinha D, Koch P, Di Sanzo S, et al.
1205 Extensive remodeling of the extracellular matrix during aging contributes to age-
1206 dependent impairments of muscle stem cell functionality. *Cell Rep.* 2021;35(10):109223.
1207 17. Meyer GA, and Lieber RL. Elucidation of extracellular matrix mechanics from muscle
1208 fibers and fiber bundles. *Journal of biomechanics.* 2011;44(4):771-3.
1209 18. D'Amore A, Amoroso N, Gottardi R, Hobson C, Carruthers C, Watkins S, et al. From
1210 single fiber to macro-level mechanics: A structural finite-element model for elastomeric
1211 fibrous biomaterials. *J Mech Behav Biomed Mater.* 2014;39:146-61.
1212 19. Carleton JB, D'Amore A, Feaver KR, Rodin GJ, and Sacks MS. Geometric
1213 characterization and simulation of planar layered elastomeric fibrous biomaterials. *Acta*
1214 *Biomater.* 2015;12:93-101.
1215 20. D'Amore A, Nasello G, Luketich SK, Denisenko D, Jacobs DL, Hoff R, et al. Meso-scale
1216 topological cues influence extracellular matrix production in a large deformation,
1217 elastomeric scaffold model. *Soft Matter.* 2018;14(42):8483-95.
1218 21. Pajerowski JD, Dahl KN, Zhong FL, Sammak PJ, and Discher DE. Physical plasticity of
1219 the nucleus in stem cell differentiation. *Proc Natl Acad Sci U S A.* 2007;104(40):15619-
1220 24.
1221 22. Spagnol ST, and Dahl KN. Active cytoskeletal force and chromatin condensation
1222 independently modulate intranuclear network fluctuations. *Integr Biol (Camb).*
1223 2014;6(5):523-31.
1224 23. McQuin C, Goodman A, Chernyshev V, Kamentsky L, Cimini BA, Karhohs KW, et al.
1225 CellProfiler 3.0: Next-generation image processing for biology. *PLoS Biol.*
1226 2018;16(7):e2005970.

1227 24. Heckenbach I, Mkrtchyan GV, Ezra MB, Bakula D, Madsen JS, Nielsen MH, et al.
1228 Nuclear morphology is a deep learning biomarker of cellular senescence.
1229 25. Meschiari CA, Ero OK, Pan H, Finkel T, and Lindsey ML. The impact of aging on cardiac
1230 extracellular matrix. *Geroscience.* 2017;39(1):7-18.
1231 26. Willett TL, Dapaah DY, Uppuganti S, Granke M, and Nyman JS. Bone collagen network
1232 integrity and transverse fracture toughness of human cortical bone. *Bone.* 2019;120:187-
1233 93.
1234 27. Aicher BO, Zhang J, Muratoglu SC, Galisteo R, Arai AL, Gray VL, et al. Moderate
1235 aerobic exercise prevents matrix degradation and death in a mouse model of aortic
1236 dissection and aneurysm. *Am J Physiol Heart Circ Physiol.* 2021;320(5):H1786-h801.
1237 28. Spengler DM, Baylink DJ, and Rosenquist JB. Effect of beta-aminopropionitrile on bone
1238 mechanical properties. *J Bone Joint Surg Am.* 1977;59(5):670-2.
1239 29. Iijima H, Gilmer G, Wang K, Bean AC, He Y, Lin H, et al. Age-related matrix stiffening
1240 epigenetically regulates α-Klotho expression and compromises chondrocyte integrity.
1241 *Nat Commun.* 2023;14(1):18.
1242 30. Trapnell C, Cacchiarelli D, Grimsby J, Pokharel P, Li S, Morse M, et al. The dynamics
1243 and regulators of cell fate decisions are revealed by pseudotemporal ordering of single
1244 cells. *Nat Biotechnol.* 2014;32(4):381-6.
1245 31. Qiu X, Hill A, Packer J, Lin D, Ma YA, and Trapnell C. Single-cell mRNA quantification
1246 and differential analysis with Census. *Nat Methods.* 2017;14(3):309-15.
1247 32. Bentzinger CF, Wang YX, Maltzahn J, Soleimani VD, Yin H, and Rudnicki M. Fibronectin
1248 regulates Wnt7a signaling and satellite cell expansion. *Cell Stem Cell.* 2013;12.
1249 33. Baldin V, Lukas J, Marcote MJ, Pagano M, and Draetta G. Cyclin D1 is a nuclear protein
1250 required for cell cycle progression in G1. *Genes Dev.* 1993;7(5):812-21.
1251 34. Charge SB, and Rudnicki MA. Cellular and molecular regulation of muscle regeneration.
1252 *Physiol Rev.* 2004;84(1):209-38.
1253 35. Núñez-Álvarez Y, Hurtado E, Muñoz M, García-Tuñon I, Rech GE, Pluvinet R, et al.
1254 Loss of HDAC11 accelerates skeletal muscle regeneration in mice. *Febs j.*
1255 2021;288(4):1201-23.
1256 36. Edfors F, Danielsson F, Hallström BM, Käll L, Lundberg E, Pontén F, et al. Gene-specific
1257 correlation of RNA and protein levels in human cells and tissues. *Mol Syst Biol.*
1258 2016;12(10):883.

1259 37. Gry M, Rimini R, Strömberg S, Asplund A, Pontén F, Uhlén M, et al. Correlations
1260 between RNA and protein expression profiles in 23 human cell lines. *BMC Genomics.*
1261 2009;10(1):365.
1262 38. Liu Y, Beyer A, and Aebersold R. On the Dependency of Cellular Protein Levels on
1263 mRNA Abundance. *Cell.* 2016;165(3):535-50.
1264 39. Bevilacqua A, Ceriani MC, Capaccioli S, and Nicolin A. Post-transcriptional regulation of
1265 gene expression by degradation of messenger RNAs. *J Cell Physiol.* 2003;195(3):356-
1266 72.
1267 40. La Manno G, Soldatov R, Zeisel A, Braun E, Hochgerner H, Petukhov V, et al. RNA
1268 velocity of single cells. *Nature.* 2018;560(7719):494-8.
1269 41. Qiu X, Zhang Y, Martin-Rufino JD, Weng C, Hosseinzadeh S, Yang D, et al. Mapping
1270 transcriptomic vector fields of single cells. *Cell.* 2022;185(4):690-711.e45.
1271 42. Díaz-Uriarte R, and Alvarez de Andrés S. Gene selection and classification of microarray
1272 data using random forest. *BMC Bioinformatics.* 2006;7(1):3.
1273 43. Wek RC. Role of eIF2α Kinases in Translational Control and Adaptation to Cellular
1274 Stress. *Cold Spring Harb Perspect Biol.* 2018;10(7).
1275 44. Tikhonova EB, Gutierrez Guarnizo SA, Kellogg MK, Karamyshev A, Dozmorov IM,
1276 Karamysheva ZN, et al. Defective Human SRP Induces Protein Quality Control and
1277 Triggers Stress Response. *J Mol Biol.* 2022;434(22):167832.
1278 45. Gille H, Strahl T, and Shaw PE. Activation of ternary complex factor Elk-1 by stress-
1279 activated protein kinases. *Curr Biol.* 1995;5(10):1191-200.
1280 46. Bresson S, Shchepachev V, Spanos C, Turowski TW, Rappsilber J, and Tollervey D.
1281 Stress-Induced Translation Inhibition through Rapid Displacement of Scanning Initiation
1282 Factors. *Mol Cell.* 2020;80(3):470-84.e8.
1283 47. Matys V, Kel-Margoulis OV, Fricke E, Liebich I, Land S, Barre-Dirrie A, et al.
1284 TRANSFAC and its module TRANSCompel: transcriptional gene regulation in
1285 eukaryotes. *Nucleic Acids Res.* 2006;34(Database issue):D108-10.
1286 48. Bernet JD, Doles JD, Hall JK, Kelly Tanaka K, Carter TA, and Olwin BB. p38 MAPK
1287 signaling underlies a cell-autonomous loss of stem cell self-renewal in skeletal muscle of
1288 aged mice. *Nat Med.* 2014;20(3):265-71.
1289 49. Durand S, Cougot N, Mahuteau-Betzer F, Nguyen CH, Grierson DS, Bertrand E, et al.
1290 Inhibition of nonsense-mediated mRNA decay (NMD) by a new chemical molecule
1291 reveals the dynamic of NMD factors in P-bodies. *J Cell Biol.* 2007;178(7):1145-60.

1292 50. Hug N, Longman D, and Cáceres JF. Mechanism and regulation of the nonsense-
1293 mediated decay pathway. *Nucleic Acids Res.* 2016;44(4):1483-95.
1294 51. Wallmeroth D, Lackmann J-W, Kueckelmann S, Altmüller J, Dieterich C, Boehm V, et al.
1295 Human UPF3A and UPF3B enable fault-tolerant activation of nonsense-mediated mRNA
1296 decay. *The EMBO Journal.* 2022;41(10):e109191.
1297 52. Hu G, Cui K, Northrup D, Liu C, Wang C, Tang Q, et al. H2A.Z facilitates access of
1298 active and repressive complexes to chromatin in embryonic stem cell self-renewal and
1299 differentiation. *Cell Stem Cell.* 2013;12(2):180-92.
1300 53. Huh YH, Noh M, Burden FR, Chen JC, Winkler DA, and Sherley JL. Sparse feature
1301 selection identifies H2A.Z as a novel, pattern-specific biomarker for asymmetrically self-
1302 renewing distributed stem cells. *Stem Cell Res.* 2015;14(2):144-54.
1303 54. Tanaka KK, Hall JK, Troy AA, Cornelison DD, Majka SM, and Olwin BB. Syndecan-4-
1304 expressing muscle progenitor cells in the SP engraft as satellite cells during muscle
1305 regeneration. *Cell Stem Cell.* 2009;4(3):217-25.
1306 55. Sousa-Victor P, Gutarra S, Garcia-Prat L, Rodriguez-Ubreva J, Ortet L, Ruiz-Bonilla V,
1307 et al. Geriatric muscle stem cells switch reversible quiescence into senescence. *Nature.*
1308 2014;506(7488):316-21.
1309 56. Oprescu SN, Yue F, Qiu J, Brito LF, and Kuang S. Temporal Dynamics and
1310 Heterogeneity of Cell Populations during Skeletal Muscle Regeneration. *iScience.*
1311 2020;23(4):100993.
1312 57. Cosgrove BD, Gilbert PM, Porpiglia E, Mourkioti F, Lee SP, Corbel SY, et al.
1313 Rejuvenation of the muscle stem cell population restores strength to injured aged
1314 muscles. *Nat Med.* 2014;20(3):255-64.
1315 58. Moyle LA, Cheng RY, Liu H, Davoudi S, Ferreira SA, Nissar AA, et al. Three-
1316 dimensional niche stiffness synergizes with Wnt7a to modulate the extent of satellite cell
1317 symmetric self-renewal divisions. *Molecular Biology of the Cell.* 2020;31(16):1703-13.
1318 59. Chenette DM, Cadwallader AB, Antwine TL, Larkin LC, Wang J, Olwin BB, et al.
1319 Targeted mRNA Decay by RNA Binding Protein AUF1 Regulates Adult Muscle Stem
1320 Cell Fate, Promoting Skeletal Muscle Integrity. *Cell Rep.* 2016;16(5):1379-90.
1321 60. Wheeler JR, Whitney ON, Vogler TO, Nguyen ED, Pawlikowski B, Lester E, et al. RNA-
1322 binding proteins direct myogenic cell fate decisions. *Elife.* 2022;11.
1323 61. Maeda R, Kami D, Shikuma A, Suzuki Y, Taya T, Matoba S, et al. RNA decay in
1324 processing bodies is indispensable for adipogenesis. *Cell Death Dis.* 2021;12(4):285.

1325 62. Li T, Shi Y, Wang P, Guachalla LM, Sun B, Joerss T, et al. Smg6/Est1 licenses
1326 embryonic stem cell differentiation via nonsense-mediated mRNA decay. *Embo j.*
1327 2015;34(12):1630-47.
1328 63. Abbadi D, Yang M, Chenette DM, Andrews JJ, and Schneider RJ. Muscle development
1329 and regeneration controlled by AUF1-mediated stage-specific degradation of fate-
1330 determining checkpoint mRNAs. *Proceedings of the National Academy of Sciences.*
1331 2019;116(23):11285-90.
1332 64. Blatt P, Wong-Deyrup SW, McCarthy A, Breznak S, Hurton MD, Upadhyay M, et al. RNA
1333 degradation is required for the germ-cell to maternal transition in Drosophila. *Current*
1334 *Biology.* 2021;31(14):2984-94.e7.
1335 65. Solana J, Gamberi C, Mihaylova Y, Grosswendt S, Chen C, Lasko P, et al. The CCR4-
1336 NOT complex mediates deadenylation and degradation of stem cell mRNAs and
1337 promotes planarian stem cell differentiation. *PLoS Genet.* 2013;9(12):e1004003.
1338 66. Lou CH, Chousal J, Goetz A, Shum EY, Brafman D, Liao X, et al. Nonsense-Mediated
1339 RNA Decay Influences Human Embryonic Stem Cell Fate. *Stem Cell Reports.*
1340 2016;6(6):844-57.
1341 67. Belair C, Sim S, Kim KY, Tanaka Y, Park IH, and Wolin SL. The RNA exosome nuclease
1342 complex regulates human embryonic stem cell differentiation. *J Cell Biol.*
1343 2019;218(8):2564-82.
1344 68. Di Stefano B, Luo EC, Haggerty C, Aigner S, Charlton J, Brumbaugh J, et al. The RNA
1345 Helicase DDX6 Controls Cellular Plasticity by Modulating P-Body Homeostasis. *Cell*
1346 *Stem Cell.* 2019;25(5):622-38.e13.
1347 69. Hausburg MA, Doles JD, Clement SL, Cadwallader AB, Hall MN, Blackshear PJ, et al.
1348 Post-transcriptional regulation of satellite cell quiescence by TTP-mediated mRNA
1349 decay. *Elife.* 2015;4:e03390.
1350 70. Chen Y-F, Li Y-SJ, Chou C-H, Chiew MY, Huang H-D, Ho JH-C, et al. Control of matrix
1351 stiffness promotes endodermal lineage specification by regulating SMAD2/3 via lncRNA
1352 LINC00458. *Science Advances.* 2020;6(6):eaay0264.
1353 71. Brielle S, Bavli D, Motzik A, Kan-Tor Y, Sun X, Kozulin C, et al. Delineating the
1354 heterogeneity of matrix-directed differentiation toward soft and stiff tissue lineages via
1355 single-cell profiling. *Proceedings of the National Academy of Sciences.*
1356 2021;118(19):e2016322118.
1357 72. Trappmann B, Gautrot JE, Connelly JT, Strange DG, Li Y, Oyen ML, et al. Extracellular-
1358 matrix tethering regulates stem-cell fate. *Nat Mater.* 2012;11(7):642-9.

1359 73. Selman M, and Pardo A. Fibroageing: An ageing pathological feature driven by
1360 dysregulated extracellular matrix-cell mechanobiology. *Ageing Res Rev.*
1361 2021;70:101393.
1362 74. Rivera T, Haggblom C, Cosconati S, and Karlseder J. A balance between elongation
1363 and trimming regulates telomere stability in stem cells. *Nat Struct Mol Biol.*
1364 2017;24(1):30-9.
1365 75. Liang J, Balachandra S, Ngo S, and O'Brien LE. Feedback regulation of steady-state
1366 epithelial turnover and organ size. *Nature.* 2017;548(7669):588-91.
1367 76. Mendell JT, Sharifi NA, Meyers JL, Martinez-Murillo F, and Dietz HC. Nonsense
1368 surveillance regulates expression of diverse classes of mammalian transcripts and
1369 mutes genomic noise. *Nat Genet.* 2004;36(10):1073-8.
1370 77. Goetz AE, and Wilkinson M. Stress and the nonsense-mediated RNA decay pathway.
1371 *Cell Mol Life Sci.* 2017;74(19):3509-31.
1372 78. Pakos-Zebrucka K, Koryga I, Mnich K, Ljujic M, Samali A, and Gorman AM. The
1373 integrated stress response. *EMBO Rep.* 2016;17(10):1374-95.
1374 79. Karam R, Lou CH, Kroeger H, Huang L, Lin JH, and Wilkinson MF. The unfolded protein
1375 response is shaped by the NMD pathway. *EMBO Rep.* 2015;16(5):599-609.
1376 80. Deng M, Lin J, Nowsheen S, Liu T, Zhao Y, Villalta PW, et al. Extracellular matrix
1377 stiffness determines DNA repair efficiency and cellular sensitivity to genotoxic agents.
1378 *Sci Adv.* 2020;6(37).
1379 81. Holstein EM, Clark KR, and Lydall D. Interplay between nonsense-mediated mRNA
1380 decay and DNA damage response pathways reveals that Stn1 and Ten1 are the key
1381 CST telomere-cap components. *Cell Rep.* 2014;7(4):1259-69.
1382 82. Stoneley M, Harvey RF, Mulroney TE, Mordue R, Jukes-Jones R, Cain K, et al.
1383 Unresolved stalled ribosome complexes restrict cell-cycle progression after genotoxic
1384 stress. *Molecular Cell.* 2022;82(8):1557-72.e7.
1385 83. Wong ES, Le Guezennec X, Demidov ON, Marshall NT, Wang ST, Krishnamurthy J, et
1386 al. p38MAPK controls expression of multiple cell cycle inhibitors and islet proliferation
1387 with advancing age. *Dev Cell.* 2009;17(1):142-9.
1388 84. Perdiguero E, Ruiz-Bonilla V, Gresh L, Hui L, Ballestar E, Sousa-Victor P, et al. Genetic
1389 analysis of p38 MAP kinases in myogenesis: fundamental role of p38alpha in abrogating
1390 myoblast proliferation. *Embo j.* 2007;26(5):1245-56.
1391 85. Wang C, Schmich F, Srivatsa S, Weidner J, Beerenwinkel N, and Spang A. Context-
1392 dependent deposition and regulation of mRNAs in P-bodies. *eLife.* 2018;7:e29815.

1393 86. Pecori F, Kondo N, Ogura C, Miura T, Kume M, Minamijima Y, et al. Site-specific O-
1394 GlcNAcylation of Psme3 maintains mouse stem cell pluripotency by impairing P-body
1395 homeostasis. *Cell Rep.* 2021;36(2):109361.
1396 87. Lipsitz LA, and Goldberger AL. Loss of 'complexity' and aging. Potential applications of
1397 fractals and chaos theory to senescence. *Jama.* 1992;267(13):1806-9.
1398 88. Jaiswal S, and Ebert BL. Clonal hematopoiesis in human aging and disease. *Science.*
1399 2019;366(6465).
1400 89. Hernando-Herraez I, Evano B, Stubbs T, Commere P-H, Jan Bonder M, Clark S, et al.
1401 Ageing affects DNA methylation drift and transcriptional cell-to-cell variability in mouse
1402 muscle stem cells. *Nature Communications.* 2019;10(1):4361.
1403 90. Clemens Z, Sivakumar S, Pius A, Sahu A, Shinde S, Mamiya H, et al. The biphasic and
1404 age-dependent impact of klotho on hallmarks of aging and skeletal muscle function.
1405 *eLife.* 2021;10:e61138.
1406 91. Li X, Ploner A, Wang Y, Magnusson PKE, Reynolds C, Finkel D, et al. Longitudinal
1407 trajectories, correlations and mortality associations of nine biological ages across 20-
1408 years follow-up. *eLife.* 2020;9:e51507.
1409 92. Tuck AC, Rankova A, Arpat AB, Liechti LA, Hess D, Iesmantavicius V, et al. Mammalian
1410 RNA Decay Pathways Are Highly Specialized and Widely Linked to Translation.
1411 *Molecular Cell.* 2020;77(6):1222-36.e13.
1412 93. Smalec BM, Ietswaart R, Choquet K, McShane E, West ER, and Churchman LS.
1413 Genome-wide quantification of RNA flow across subcellular compartments reveals
1414 determinants of the mammalian transcript life cycle. *bioRxiv.* 2022:2022.08.21.504696.
1415 94. Lashkevich KA, and Dmitriev SE. mRNA Targeting, Transport and Local Translation in
1416 Eukaryotic Cells: From the Classical View to a Diversity of New Concepts. *Mol Biol.*
1417 2021;55(4):507-37.
1418 95. Sahu A, Clemens ZJ, Shinde SN, Sivakumar S, Pius A, Bhatia A, et al. Regulation of
1419 aged skeletal muscle regeneration by circulating extracellular vesicles. *Nature Aging.*
1420 2021;1(12):1148-61.
1421 96. Stylianopoulos T, and Barocas VH. Multiscale, structure-based modeling for the elastic
1422 mechanical behavior of arterial walls. *J Biomech Eng.* 2007;129(4):611-8.
1423 97. D'Amore A, Stella JA, Wagner WR, and Sacks MS. Characterization of the complete
1424 fiber network topology of planar fibrous tissues and scaffolds. *Biomaterials.*
1425 2010;31(20):5345-54.

1426 98. Zhao F, Xiong Y, Ito K, van Rietbergen B, and Hofmann S. Porous Geometry Guided
1427 Micro-mechanical Environment Within Scaffolds for Cell Mechanobiology Study in Bone
1428 Tissue Engineering. *Front Bioeng Biotechnol.* 2021;9:736489.
1429 99. Smith LR, Hammers DW, Sweeney HL, and Barton ER. Increased collagen cross-linking
1430 is a signature of dystrophin-deficient muscle. *Muscle Nerve.* 2016;54(1):71-8.
1431 100. Mula J, Lee JD, Liu F, Yang L, and Peterson CA. Automated image analysis of skeletal
1432 muscle fiber cross-sectional area. *J Appl Physiol (1985).* 2013;114(1):148-55.
1433 101. Liu L, Cheung TH, Charville GW, and Rando TA. Isolation of skeletal muscle stem cells
1434 by fluorescence-activated cell sorting. *Nat Protoc.* 2015;10(10):1612-24.
1435 102. Soneson C, and Robinson MD. Bias, robustness and scalability in single-cell differential
1436 expression analysis. *Nat Methods.* 2018;15(4):255-61.
1437 103. Hettinger ZR, Wen Y, Peck BD, Hamagata K, Confides AL, Van Pelt DW, et al.
1438 Mechanotherapy Reprograms Aged Muscle Stromal Cells to Remodel the Extracellular
1439 Matrix during Recovery from Disuse. *Function (Oxf).* 2022;3(3):zqac015.
1440 104. Rocheteau P, Gayraud-Morel B, Siegl-Cachedenier I, Blasco MA, and Tajbakhsh S. A
1441 subpopulation of adult skeletal muscle stem cells retains all template DNA strands after
1442 cell division. *Cell.* 2012;148(1-2):112-25.
1443 105. Xing J. Reconstructing data-driven governing equations for cell phenotypic transitions:
1444 integration of data science and systems biology. *Physical Biology.* 2022;19(6):061001.
1445 106. Reimand J, Isserlin R, Voisin V, Kucera M, Tannus-Lopes C, Rostamianfar A, et al.
1446 Pathway enrichment analysis and visualization of omics data using g:Profiler, GSEA,
1447 Cytoscape and EnrichmentMap. *Nat Protoc.* 2019;14(2):482-517.
1448 107. Svensson V, Natarajan KN, Ly L-H, Miragaia RJ, Labalette C, Macaulay IC, et al. Power
1449 analysis of single-cell RNA-sequencing experiments. *Nature Methods.* 2017;14(4):381-7.
1450